Sentinel-5 Precursor + Innovation: Sentinel-5 Precursor Ocean Color (S5POC)

Algorithm Theoretical Base Document (ATBD)

Date: Sep 30, 2025

A. Bracher[1,2] J. Oelker[1,2] A. J. Bellido Rosas[1,2] A. Richter[2]

[1]Alfred Wegener Institute (AWI), Helmholtz Centre for Polar and Marine Research, Bussestraße 24, D-27570 Bremerhaven, Germany

[2]Institute of Environmental Physics (IUP), University of Bremen, Otto-Hahn-Allee 1, D-28359 Bremen, Germany

Change log

Version Nr.	Date	Status	Change
1.0	Nov 7, 2024	Draft ATBDv1	First Draft
1.1	Sep 30, 2025	ATBDv1.1	New variables added, LUT updated

Contents

List of Figures

List of Tables

List of Abbreviations

AOD Aerosol Optical Depth

AWI Alfred Wegener Institute Helmholtz Centre for Polar and Marine Research

CDOM Colored dissolved organic matter

CCD Charge-coupled device

Chla Chlorophyll-a concentration

DOAS Differential Optical Absorption Spectroscopy

fMSE fractional mean squared error

GOME-2 Global Ozone Monitoring Experiment-2

HITRAN High-resolution transmission molecular absorption database

IOP Inherent Optical Properties

IUP Institute of Environmental Physics

K_d Diffuse attenuation coefficient

LUT Look-up Table

MAE Mean absolute error

MODIS-Aqua Moderate Resolution Imaging Spectroradiometer-Aqua

NIR Near-infrared

OC-PFT Algorithm of Hirata et al. (2011) to retrieve phytoplankton functional types

OLCI Ocean and Land Colour Instrument

OMI Ozone Monitoring Instrument

PACE Plankton, Aerosol, Cloud and ocean Ecosystem

PFT Phytoplankton Functional Type

PhytoDOAS DOAS applied for retrieval of phytoplankton biomass

RB	Requirements Baseline
RMSD	Root mean squared difference
RRS	Rotational Raman Scattering
RTM	Radiative Transfer Model
S5P	Sentinel-5 Precursor
S5POC	Sentinel-5 Precursor Ocean Color
SCIAMACHY	Scanning Imaging Absorption Spectrometers for Atmospheric Chartography
SIF-marine	sun induced marine Chla fluorescence
SWIR	Shortwave infrared
SynSenPFT	Synergistic Exploitation of hyper- and multispectral Sentinel measurements to determine Phytoplankton Functional Types
SZA	Solar zenith angle
TC	Triple collocation
TChla	Total chlorophyll-a concentration
TOA	Top of Atmosphere
TROPOMI	Tropospheric Monitoring Instrument
UV	Ultraviolet
UVA	DOAS fit window in ultraviolet-A from 356.5 to 390 nm
UVAB	DOAS fit window in ultraviolet-A from 312.5 to 338.5 nm
VIS	Visible
VRS	Vibrational Raman Scattering
VZA	Viewing Zenith Angle

1 Document Overview

This document describes the theoretical basis and implementation of the Sentinel-5P Ocean Color (S5POC) level-2 TROPOMI products. Section 2 describes the TROPOMI instrument. Sentinel-5P Ocean Color (S5POC) level-2 TROPOMI products include the diffuse attenuation coefficients (Kd) at the UV-AB, UV-A and short blue wavelength range based on (Oelker *et al.*, 2022b). These products are introduced in section 3. A detailed description of the S5POC Kd level 2 product algorithm follows in section 4. Feasibility of an operational processing of the S5POC products is discussed in section 5. Section 6 presents the methods used to calculate uncertainties for the products. Validation with *in situ* data is summed up in section 7.

2 TROPOMI instrument

The satellite Sentinel-5 Precursor (S5P) hosts the Tropospheric Monitoring Instrument (TROPOMI) (Veefkind *et al.*, 2012). It is in a low Earth orbit and its standard level 2 products provide daily global measurements of atmospheric trace gases and aerosols. The satellite was launched in October 2017. Local solar time at ascending node is 13:30. TROPOMI measures backscattered radiances at a spatial resolution of 3.5 km by 5.5 km (until 5 August 2019 at 3.5 km by 7 km) at nadir. Once per day the solar irradiance is recorded. Measurements are taken by a charge-coupled device (CCD) sensor at a swath width of 2600 km providing daily global coverage. TROPOMI has spectral bands in the ultraviolet (UV), the visible (VIS), near-infrared (NIR), and the shortwave infrared (SWIR). Relevant for developing ocean color products are band 3 (UV) from 310 nm to 405 nm, and band 4 (VIS) from 405 nm to 500 nm. The spectral resolution is 0.55 nm for bands 3 and 4.

3 Introduction to TROPOMI diffuse attenuation coefficient products

Traditionally, ocean color products are derived from multispectral sensors that record the backscattered radiance at 8 to 21 bands with a width of 10 to 20 nm in the VIS and NIR. Current multispectral sensors with daily global coverage have a spatial resolution below 500 m. Most ocean color retrievals are based on the water-leaving radiance which is acquired from the backscattered radiance by applying an atmospheric correction. The broad spectral resolution and limited number of bands of multispectral sensors limits the discrimination of the optical imprints of different water constituents. Hyperspectral ocean color sensors that continuously record the backscattered radiance at a spectral resolution of 5 nm or lower offer a new level for observing the ocean from space. Upcoming hyperspectral ocean color sensors such as the Plankton, Aerosol, Cloud and ocean Ecosystem (PACE) mission (https://pace.oceansciences.org/mission.htm) target a better spectral resolution of 5 nm which will allow for a better understanding of the phytoplankton ecology.

Atmospheric sensors measure the backscattered radiance at much higher spectral resolution, around 0.5 nm in the UV to NIR bands. It has been shown that measurements from these kind of sensors can be exploited to successfully retrieve phytoplankton functional types (Bracher *et al.*, 2009; Sadeghi *et al.*, 2012), light availability (Dinter *et al.*, 2015), diffuse attenuation (Dinter *et al.*, 2015; Oelker *et al.*, 2019, 2022b), and sun-induced marine fluorescence (Wolanin *et al.*, 2015a; Joiner & Vasilkov, 2006). Spatial resolution of atmospheric sensors has advanced. TROPOMI sets a new record in spatial resolution with 3.5 km by 5.5 km (3.5 km by 5.5 km until 5 Aug 2019) and correspondingly this is the resolution of TROPOMI level-1 and level-2 products.

The S5POC project exploited TROPOMI's potential for retrieving ocean color products. This helps not only for obtaining hyperspectrally-derived ocean color data sets in time periods where no hyperspectral ocean color missions are available and adds understanding for hyperspectral ocean color retrievals, but also offers unique ocean color retrievals by exploiting the filling-in of Fraunhofer structures by vibrational Raman scattering (VRS) which requires a spectral resolution below 1 nm. Within S5POC-PAL the algorithm developed within S5POC for the diffuse attenuation coefficients (K_d) in the UV-AB, UV-A and short blue wavelength range by (Oelker *et al.*, 2022b) is implemented and is described in detail within this document. The retrieval is based on the Differential Optical Absorption Spectroscopy (DOAS) in combination with radiative transfer modeling (RTM). S5POC TROPOMI products are produced at TROPOMI's level-1 and level-2 product resolution.

3.1 Introducing diffuse attenuation

The diffuse attenuation coefficient (K_d) is important for understanding biogeochemical processes and the heat budget of the global ocean. It describes how fast the incoming radiation diminishes with ocean depth z and can be calculated as a mean value over distant depths z_1 and z_2 from the change in downwelling irradiance $E_d(z)$ (Lee *et al.*, 2005)

$$K_d(z_1 \longleftrightarrow z_2, \lambda) = \frac{1}{z_2 - z_1} \ln\left(\frac{E_d(z_1, \lambda)}{E_d(z_2, \lambda)}\right). \quad (1)$$

which gives $K_d(z_{90}, \lambda) = 1/z_{90}(\lambda)$ for the attenuation depth z_{90} defined as the depth at which the downwelling irradiance has reduced to 1/e of its subsurface value (Gordon & McCluney, 1975).

In principle, three approaches exist to estimate K_d from multispectral ocean color sensors, two empirical and one semi-analytical. The direct one-step empirical method determines K_d from the empirical relationship between K_d and the ratio of water-leaving radiances at two wavelengths in the blue and the green (Austin & Petzold, 1981). The two-step empirical approach first determines Chla from remote sensing reflectance using a standard ocean color retrieval (O'Reilly *et al.*, 1998) and then evaluates K_d using another set of empirical relationships (Morel, 1988; Morel & Maritorena, 2001). A more recent publication presents a combination of the two empirical approaches based on ratios of water-leaving reflectances using Chla as an implicit intermediary (Morel *et al.*, 2007). The third approach first determines inherent optical properties (IOPs), i.e., absorption and backscattering, via a quasi-analytical approach in a first step and then relates these to K_d using a LUT established through extensive radiative transfer modeling (Lee *et al.*, 2005).

The K_d retrieval in the S5POC project is based on the work by Dinter *et al.* (2015) and Oelker *et al.* (2019) and details on the method, retrieval results and their validation and uncertainties can be found in the publication Oelker *et al.* (2022b). K_d is determined from the VRS signal at the top of atmosphere. VRS occurs in liquid water when vibrational modes of the water molecules are excited by inelastic scattering with photons. Incoming radiation at a single wavelength is shifted in this process and emitted as a broad band at longer wavelengths (Stokes line). Anti-Stokes line is not considered. The mean shift from excitation to emission can be described as a constant change in wave number of around $\Delta\nu = 3357\,\text{cm}^{-1}$ with a width of the broad band emission of $821\,\text{cm}^{-1}$ (Walrafen, 1967). VRS leads to filling-in of Fraunhofer lines, which can be detected as pseudo-absorption in backscattered radiances measured by hyperspectral satellites using DOAS (Vountas *et al.*, 2003). Dinter *et al.* (2015) found a relationship between the VRS at the top of atmosphere and the light availability or the diffuse attenuation coefficient in the ocean. In general, there is a close relationship between the number of inelastic scattering processes and the number of photons in the ocean and so the amount of light. RTM simulations are made of underwater radiant fluxes used to calculate K_d for a given scenario and of top of atmosphere radiances used to determine the VRS signal for a given scenario. RTM results are combined in a LUT relating K_d to VRS DOAS output. VRS DOAS results are then converted to K_d using satellite viewing geometry as additional input parameters in the LUT.

K_d is derived in three spectral regions: in the blue from 390 nm to 423 nm, in the UV-A from 356.5 nm to 390 nm (UVA), and in the UV-A from 312.5 nm to 338.5 nm (UVAB). These spectral regions correspond for K_d-blue to a blue DOAS fit window (450 nm to 493 nm) which has already been used in Losa *et al.* (2017) and Oelker *et al.* (2019) and for K_d-UVAB to a UV DOAS fit window (349.5 nm to 382 nm) already used in Vountas et al. Vountas *et al.* (2003, 2007). Extending the UV DOAS fit window to 395 nm was also tested to fully exploit the longer wavelengths available in band 3. However, fit results are more stable for the shorter wavelength window (until 382 nm). The K_d-UVA corresponds to a fit window from 405 nm to 450 nm (short-blue) which is tested for the first time. RTM settings closely follow Oelker *et al.* (2019), however, a more realistic atmosphere including more trace gases is used.

4 Algorithms for S5POC level-2 products

4.1 Cloud Screening

Clouds shield the radiance signal from the ocean, so the TROPOMI data set was filtered for cloud-free scenes using a cloud fraction of 0.01 as threshold. Cloud fractions were taken from the FRESCO type cloud retrieval in the nitrogen dioxide fit window (van Geffen *et al.*, 2019). Pixels over land and inland waters were removed from the data set, but are contained in the prototype products and flagged accordingly, see S5POC PUM (Oelker *et al.*, 2022a) for details.

4.2 Differential Optical Absorption Spectroscopy

Differential Optical Absorption Spectroscopy (DOAS) is a technique commonly used for the retrieval of atmospheric trace gases by distinguishing their high frequency absorption features (Perner & Platt, 1979). The DOAS method has been extended for investigating oceanic variables (PhytoDOAS). The amount of VRS (Vountas *et al.*, 2007), light availability (Dinter *et al.*, 2015) and K_d (Oelker *et al.*, 2019), Chla of different PFTs (Bracher *et al.*, 2009; Sadeghi *et al.*, 2012) and sun induced marine Chla fluorescence (SIF-marine) (Wolanin *et al.*, 2015a) have been successfully retrieved from SCIAMACHY and partly (SIF-marine and K_d) from OMI and/or GOME-2 measurements.

DOAS is based on Beer-Lambert's law. The PhytoDOAS approach can be formulated as:

$$\tau(\lambda) = \ln(I_0/I)$$
$$= \sum_{i=1}^{I} S_{a,i}\sigma_{a,i}(\lambda) + \sum_{j=1}^{J} S_{p,j}\sigma_{p,j}(\lambda) + \sum_{k=1}^{K} S_{s,k}\sigma_{s,k} + S_R\sigma_R$$
$$- \sum_{l=1}^{L} S_{e,l}\sigma_{e,l} + \sum_{m=0}^{M} x_m\lambda^m \quad (2)$$

where τ is the optical depth calculated as the natural logarithm of the solar irradiance I_0 and the backscattered radiance I measured by the satellite. The optical depth is a sum of all contributions from constituents in the atmosphere and ocean that modify the intensity by scattering or absorption. Absorption in the atmosphere is accounted for by a sum over I atmospheric absorbers with an optical depth calculated as product of slant column density $S_{a,i}$ and absorption cross section $\sigma_{a,i}$. The slant column density is the number density of the absorber integrated along the effective light path through the atmosphere. Likewise, $S_{p,j}$ are the slant columns or scaling factors of J oceanic absorbers with absorption cross sections $\sigma_{p,j}$. Inelastic scattering effects in the ocean are described by scaling factors $S_{s,k}$ and inelastic reference spectra $\sigma_{s,k}$. Atmospheric inelastic scattering is known as the Ring effect caused by rotational Raman scattering (RRS). S_R and σ_R are the scaling factor and reference spectrum for the Ring effect, respectively. Instrumental effects caused, e.g. by straylight in the instrument, can also be included using reference spectra $\sigma_{e,l}$ that characterize the spectral structure of, e.g. the straylight. $S_{e,l}$ are the corresponding scaling factors. A low order polynomial, typically $M < 5$, is added to account for all broad band effects such as elastic scattering in atmosphere and ocean and colored dissolved organic matter (CDOM) and non-algae particle absorption in the ocean. Eq. 2 is solved by Levenberg Marquardt least squares minimization solving for the various scaling or fit factors S and the polynomial coefficients x_m.

Inelastic scattering processes lead to filling-in of Fraunhofer lines. They are treated as pseudo-absorbers in DOAS, with their reference spectra calculated from RTM radiances including I^+ and excluding inelastic processes I^-:

$$\sigma_s = \ln \frac{I^+}{I^-} \quad (3)$$

In the atmosphere as well as in the ocean, inelastic scattering processes are present. In the ocean, fluorescence and VRS are the two important processes that are investigated for the retrieval of the products within the S5POC project.

The DOAS method can be used in small, only a few nanometer wide, wavelength windows, but also in larger wavelength windows, tens of nanometer wide, depending on the target. Only absorbing constituents and scattering processes relevant in these wavelength windows have to be considered in the DOAS fit.

The scaling or fit factors obtained for the target constituent have to be converted into a physical value, e.g. Chla. This conversion is done with the help of LUTs based on RTM simulations.

4.3 Radiative transfer model simulations

The ocean-atmosphere coupled RTM SCIATRAN (Blum *et al.*, 2012; Rozanov *et al.*, 2014, 2017) version 4.7.4 is used for simulations which are used for calculating reference spectra and LUTs and evaluating retrieval sensitivity. The optical properties of the ocean are varied by changing the Chla (case 1 waters). Other optically active constituents such as CDOM change proportionally. Top of Atmosphere (TOA) radiances are modeled for 23 different case-1 scenarios with Chla ranging between 0 and 30 mg/m^3. A standard case-1 model is used based on phytoplankton absorption in water according to (Bracher & Wiencke, 2000), CDOM absorption coefficient is represented as absorption by fulvic (50%) and humic (50%) acids. The spectral slopes of fulvic and humic absorption coefficients are set to 0.0194 nm^{-1} and 0.011 nm^{-1}, respectively. The absorption coefficient of this mixture at 440 nm is equal to that of CDOM absorption calculated according to (Morel & Maritorena, 2001) in the case of standard case-1 model. The chlorophyll and CDOM absorption coefficients are presented in Figure 1.

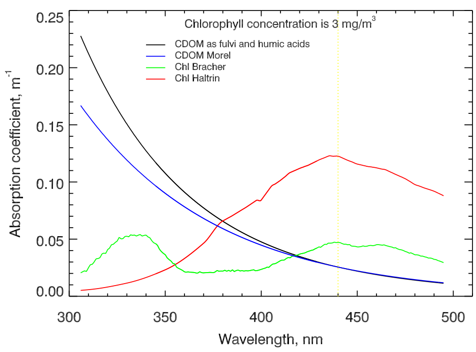

Figure 1: Comparison of chlorophyll and CDOM absorption coefficients.

A recent water absorption spectrum by Mason *et al.* (2016) is used. Particle scattering is implemented with a wavelength-independent Fournier-Forand phase function as in the widely used Hydrolight case-1 water model (Mobley & Sundman, 2013). A background maritime aerosol is assumed with aerosol optical depth (AOD) of 0.1 at 550 nm. Detailed model settings can be found in Oelker *et al.* (2022b) adapted from Oelker *et al.* (2019) and Dinter *et al.* (2015).

A TROPOMI-measured extraterrestrial solar spectrum was used for the TOA radiance calculations, since spectral alignment is very important for the DOAS retrieval. A solar spectrum measurement from a middle CCD row (row 225, 0-based) from May 2018 was chosen.

Geometry settings were chosen to cover all of TROPOMI's viewing geometries:

- TOA radiances were modeled for 13 different solar zenith angle (SZA, defined on TOA), i.e. 5° steps between 10° and 70°.
- Viewing zenith angle (VZA) was varied between 0° and 70° in steps of 5°.
- Relative azimuth angle was varied between 0° and 180° in steps of 45°.

4.4 Diffuse attenuation coefficients

K_d is derived from VRS retrieved using the PhytoDOAS method. The average K_ds are derived in three different spectral regions 312.5 to 338.5 nm (K_d-UVAB), 356.5 to 390 nm (K_d-UVA), and 390 to 423 nm (K_d-blue). Since the wavelength is shifted in the VRS process by between 35 and 60 nm in this spectral range, the three K_ds correspond to the VRS signal in three spectral regions with longer wavelengths, i.e., 349.5 to 382 nm, 405 to 450 nm, 450 to 493 nm, respectively. Since TROPOMI K_d-blue was much higher than expected an offset correction was applied to the VRS-blue fit factors. Then K_d is derived from VRS fit factors via a LUT. Details of the algorithm steps follow below and are also published in Oelker *et al.* (2022b). Figure 2 provides an overview over the K_d algorithm.

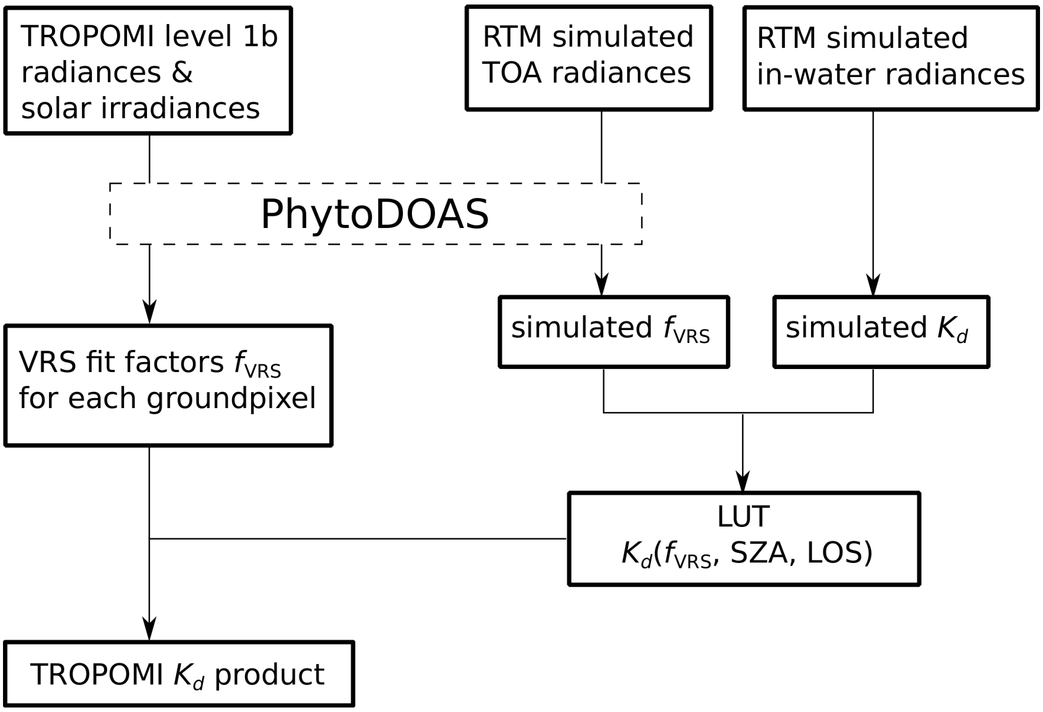

Figure 2: Flow chart illustrating the TROPOMI diffuse attenuation (K_d) algorithm. Figure from in Oelker *et al.* (2022b).

4.4.1 PhytoDOAS VRS fit

Three VRS fits are performed in three spectral regions 349.5 to 382 nm, 405 to 450 nm, and 450 to 493 nm, in the following referred to as UVA, short-blue, and blue window, respectively. The short-blue and blue windows lie in band 4 of TROPOMI's spectrometer, whereas the UVA window lies in band 3. The VRS fits in the short-blue and blue window only differ in fit window, whereas the UV window fit additionally differs in the fitted atmospheric absorbers. Considering all relevant processes in these fit windows for targeting VRS, eq. 2 reduces to:

$$\begin{aligned}\tau &= \ln \frac{I_0}{I} \\ &= \sum_{i=1}^{I} S_{a,i}\sigma_{a,i}(\lambda) + S_{VRS}\sigma_{VRS}(\lambda) - S_{OC}\sigma_{OC}(\lambda) - S_R\sigma_R(\lambda) + \sum_{m=0}^{M} x_m\lambda^m.\end{aligned} \tag{4}$$

For all three fit windows, a second order polynomial was chosen $M = 2$. The following cross sections are included in the PhytoDOAS fits for all three fit windows:

- pseudo-absorption cross section for RRS (σ_R) accounting for the Ring effect Grainger & Ring (1962) in the atmosphere. RRS pseudo-absorption cross sections are calculated based on eq. 3 Vountas *et al.* (1998).

- pseudo-absorption cross sections for VRS (σ_{VRS}) that were calculated based on eq. 3 from modeled case I TOA radiances for a Chla of 0.1 mg/m^3 and a SZA of 40°.

- ocean weighting function (σ_{OC}) defined as in Dinter *et al.* (2015) calculated from case-1 TOA radiances for a SZA of 40°. The weighting function was calculated for a change in Chla from 0.1 mg/m^3 to 0.11 mg/m^3.

Changes in SZA and Chla lead to spectral distortion of the reference spectra. Reference spectra were calculated for conditions (SZA and Chla) that lie in the middle of the ranges encountered for satellite images. Using these average conditions for calculating the spectra ensures that there is a large regime where fit factor and Chla are linearly related. Figure 3 shows the ocean weighting function and VRS reference spectrum. The impact of other phytoplankton absorption and spectral slopes of CDOM absorption coefficients does not lead to significant variations of ocean weighting function and VRS reference spectrum. As an example Figure 3 b) demonstrates comparison of curent and previous VRS pseudo-absorption spectrum.

For the blue and short-blue window, following atmospheric absorbers were fitted: absorption cross sections for ozone (O_3, Serdyuchenko *et al.*, 2014), nitrogen dioxide (NO_2, Vandaele *et al.*, 1998), water vapour (H_2O, Rothman *et al.*, 2013 using HITRAN 2009), oxygen dimer (O_4, Thalman & Volkamer, 2013). In the UVA window, the absorption cross section for bromine monoxide (BrO) was additionally fitted, but water vapour was removed from the list of absorbers.

4.4.2 Radiative transfer simulations for VRS conversion to K_d

Two types of RTM simulations have to be performed for converting VRS fit factors to K_d. On the one hand TOA radiances and on the other hand underwater radiant fluxes for various case I ocean scenarios are needed. The model should accurately describe radiative transfer processes, especially inelastic processes, in the atmosphere and in the ocean at high spectral resolution matching the spectral resolution of the satellites of about half a nanometer. The theoretical description of VRS is based on the formulation of VRS by Haltrin & Kattawar (1993). The reverse process (Anti-Stokes line) where a photon gains energy in the scattering event is much less likely in nature, since most molecules occupy the ground state. It is therefore neglected in the SCIATRAN model. Correct implementation of VRS

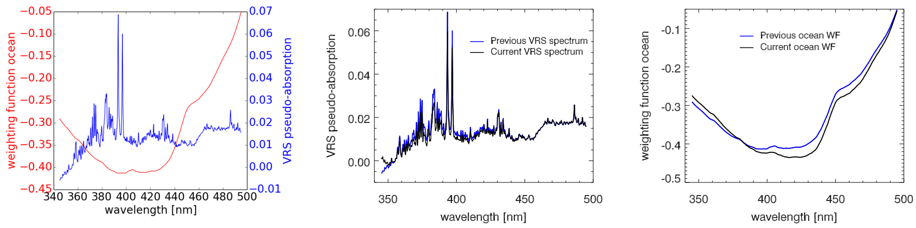

(a) (b) (c)

Figure 3: Ocean weighting function (red) and VRS reference spectrum (blue) as function of wavelength. (a) Figure adapted from Oelker *et al.* (2022b). (b) Comparison of current and previous VRS pseudo-absorption spectrum. (c) Comparison of current and previous WF ocean.

in SCIATRAN was evaluated by comparison with other radiative transfer models and experimental data from satellite, ship-based, and underwater instruments (Rozanov *et al.*, 2017). The temperature dependence of VRS was also included into the recent version of SCIATRAN software. To calculate the TOA radiances, RTM settings are chosen as described in section 4.3. Modeled TOA radiances are used to calculate VRS pseudo-absorption cross sections (eq. 3) and to perform comparative DOAS retrievals for building a LUT. Underwater fluxes are used to calculate K_d for a given model scenario. Underwater fluxes were simulated at a spectral resolution of 0.5 nm using a Fraunhofer atlas (Chance & Kurucz, 2010) since they are insensitive to the exact spectral resolution. Other model settings are the same as for the TOA radiances (section 4.3). Figure 4 illustrates simulated spectra. Figure 4 a) shows the differential optical depth as calculated from the simulated TOA radiances for different Chla. A second order polynomial was fitted to τ and subtracted. Simulated underwater fluxes are depicted in Figure 4 b) as a function of wavelength for different Chla. Figure 4 c) shows the VRS fit factors obtained with DOAS fit on these simulated differential optical depths as a function of Chla for different SZAs. The K_d averaged over the blue spectral range is shown as a function of Chla in Figure 4 d).

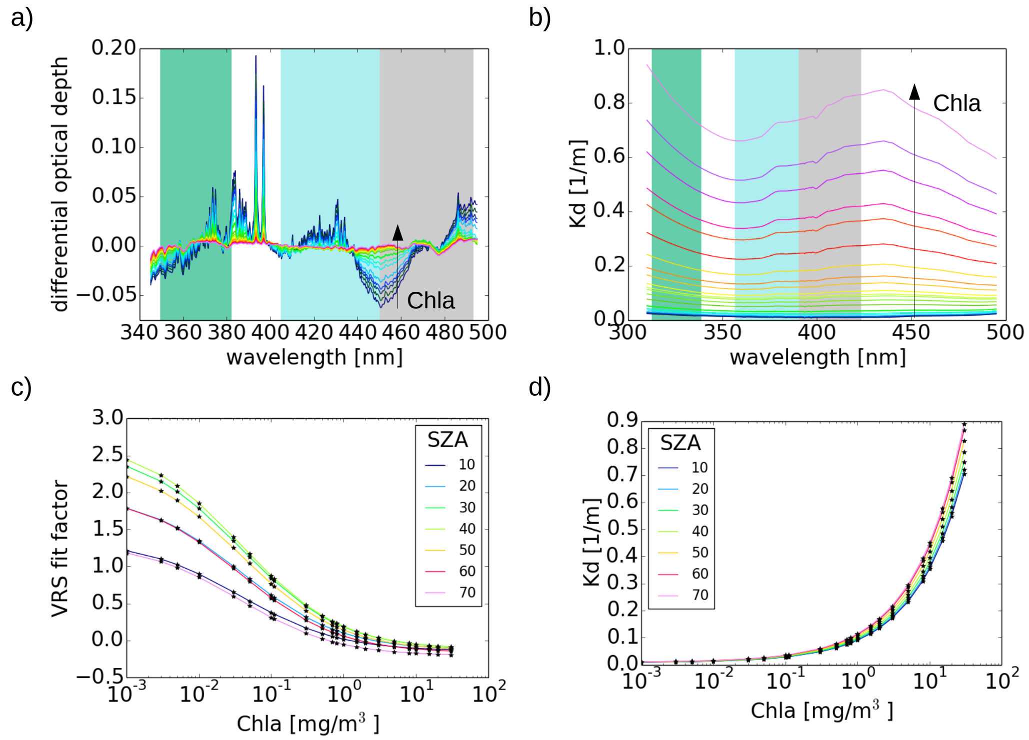

Figure 4: a) Differential optical depth as a function of wavelength for different Chla and SZA $= 40^{\circ}$ calculated from simulated TOA radiances and model-input irradiance by subtracting second order polynomial. Colored areas indicate the DOAS fit window in the blue (grey, 450-493 nm), shortblue (blue, 405-450 nm), and UV (green, 349.5-382 nm) for deriving K_d-blue, -UVA, and -UVAB, respectively. b) Spectral K_d calculated from simulated underwater fluxes for different Chla and SZA $= 40^{\circ}$. Colored areas indicate VRS excitation range over which the mean K_d is averaged (K_d-blue (390-423 nm): grey, K_d-UVA (356.5-390 nm): blue, K_d-UVAB (312.5-338.5 nm): green). c) VRS fit factor as a function of Chla as retrieved from simulated TOA radiances using DOAS. d) Mean K_d-blue, averaged in the VRS excitation range indicated by grey area in b), as a function of Chla. Black stars in c) and d) indicate the discrete Chla that were simulated, c) and d) are shown for different SZAs, VZA is 0° in all examples. Figure from Oelker *et al.* (2022b), suppl. material.

The impact of temperature on the VRS spectra and accuracy of K_d retrieval is illustrated in Figure 5. The relative difference of derived K_d^{der} from expected K_d^{exp} caused by the variation of temperature were calculated as $(K_d^{exp} - K_d^{der})/K_d^{exp}\,100$. One can see that the impact of temperature variations is below ~1% in the case of K_d-UVAB and K_d- UVA. However, in the case of K_d-blue less than ∼0.1 m^{-1} the impact of temperature variations is larger than ∼2% and increases with decreasing of K_d (see Figure 5 (c)).

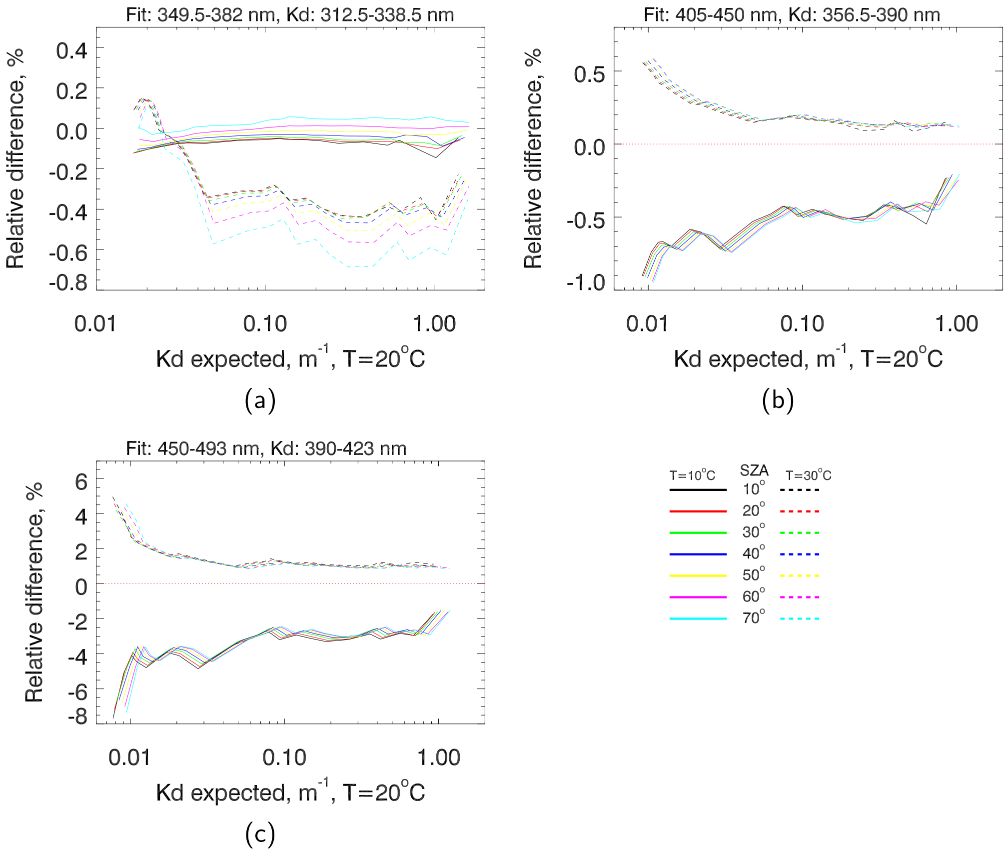

Figure 5: Relative difference between expected and derived K_d caused by temperature dependence of VRS frequency redistribution function. In the spectral range (a) [312.5 - 338.5] nm, (b) [356.5 - 390.0] nm, (c) [390.0 - 423.0] nm. Expected K_d is calculated using water temperature 20°C. Solid lines - relative difference for the water temperature equal to 10°C. Dashed lines - relative difference for the water temperature equal to 30°C.

4.4.3 LUT for deriving K_d from VRS

The LUT for deriving K_d from VRS is built by combining VRS PhytoDOAS fits on simulated TOA radiances with K_d calculated from simulated underwater radiant fluxes.

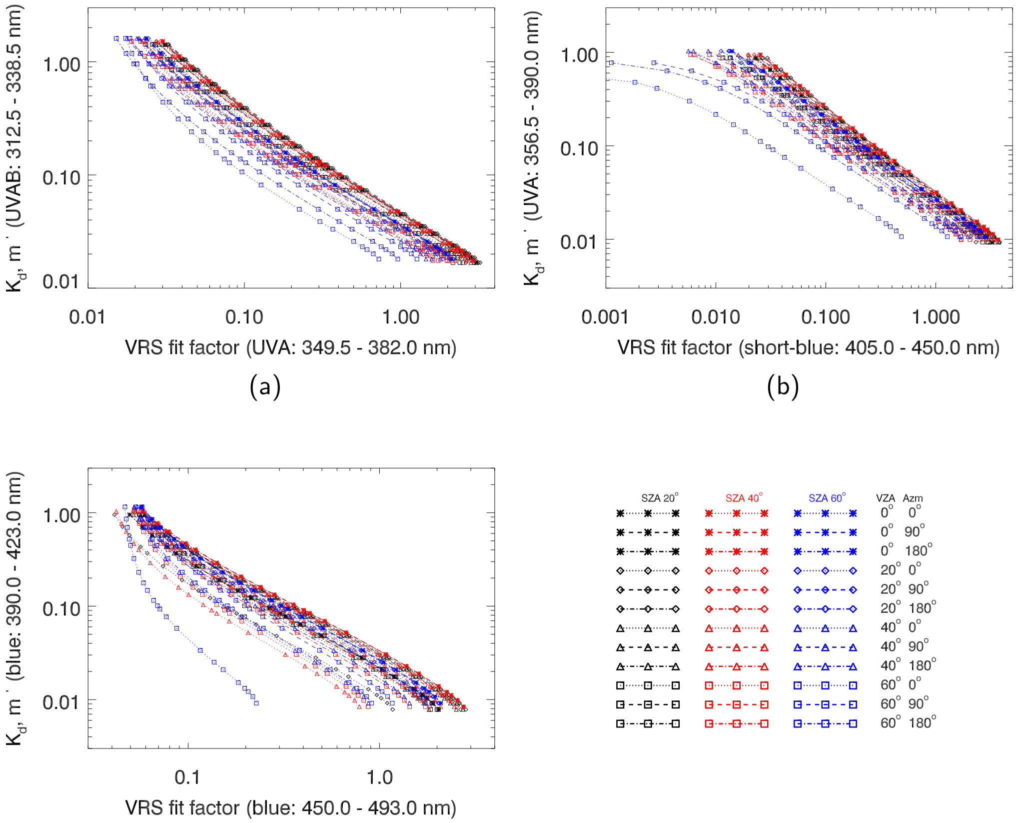

(c)

Figure 6: Look-up tables for converting VRS fit factors into diffuse attenuation coefficients for three spectral regions (a) UVAB, (b) UVA, and (c) blue. The selected SZA are shown as colors. The linestyle and symbol indicates the different VZA and azimuth angels (Azm).

DOAS fit settings for the retrieval of theoretical VRS fit factors from the modeled TOA radiances are the same as for the retrieval on satellite radiances (see section 4.4.1) except for atmospheric cross sections. Water vapour is not fitted, since it is not included in the SCIATRAN simulation. K_d is calculated according to eq. 1 for each wavelength from the underwater radiant flux simulations which give amongst others the downwelling irradiance at discrete depths z. z_{90} is determined via linear interpolation of the log-transformed downwelling irradiance E_d at depth. Resulting K_d are then averaged over wavelength between 312.5 nm and 338.5 nm for the K_d-UVAB, between 356.5 nm and 390 nm for the K_d-UVA, and between 390 nm and 423 nm for the K_d-blue. K_d calculations and VRS PhytoDOAS retrievals are performed for each SZA, VZA, and azimuth angle separately.

VRS fit factors are matched with K_d calculated from scenarios with the same Chla (combination of Figures 4 c) and d)). A four-dimensional LUT is created where K_d is a function of VRS fit factor, SZA, VZA, and azimuth angle. LUTs for K_d in the three spectral regions from the blue to the UV are shown in Figure 6. Only selected three SZAs (20°,40°,60°), fourth VZAs (0°,20°,40°,60°) and three azimuth angles (0°,90°,180°) from the range of all simulated angles are shown.

4.4.4 TROPOMI processing to VRS and Kd

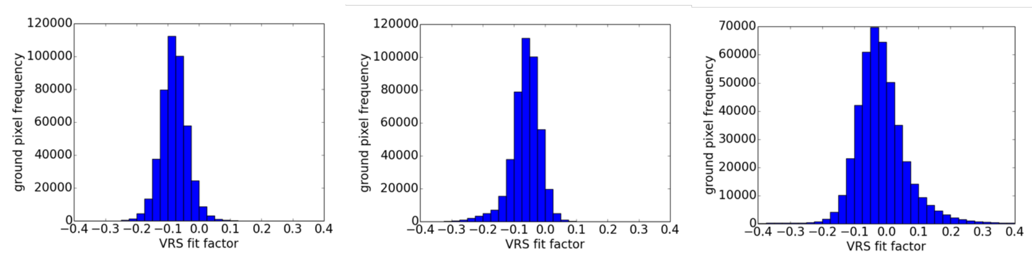

Figure 7: TROPOMI VRS-fit factor frequency distributions for the three wavelength windows (from left to right) UVA, short-blue and blue over cloudy scenes for 14 to 20 May 2018 in the Atlantic Ocean.

TROPOMI level-1b data of the time period 11 May to 9 June 2018 obtained over the Atlantic Ocean were processed (see section 4.4.1) for the three PhytoDOAS fit windows in the UV, short-blue and blue to retrieve VRS fit factors. Additionally, for investigating instrumental effects on the VRS retrievals, VRS fit factors of completely cloudy scenes were analysed. The fit factors for VRS at the three wavelengths windows (UVA, short blue and blue) were zero or very close to zero (Figure 7), which indicates that the influence of instrumental effects on the retrieval is small, opposed to GOME-2 VRS-fits, for which a large VZA dependence was found over clouds (see Oelker (2021)).

After applying the LUT as described in section 4.4.3, TROPOMI-derived K_d-blue was much higher than expected (see comparisons to K_d from in-situ and to similar satellite products in S5POC-VR, see Figure 8a). Figure 9 shows the originally retrieved VRS-blue and K_d-blue for this time period and area. Therefore, an empirical offset correction had to be developed which improved the agreement of K_d-blue to the wavelength-converted K_d(490) from OLCI and OC-CCI when a constant was added to the VRS fit factors. Generally, TROPOMI original K_d-blue is closer to the OLCI K_d-blue than the OC-CCI K_d-blue and correlation is highest for low K_d values (see Table 5 and Figure 5 in S5POC-VR).

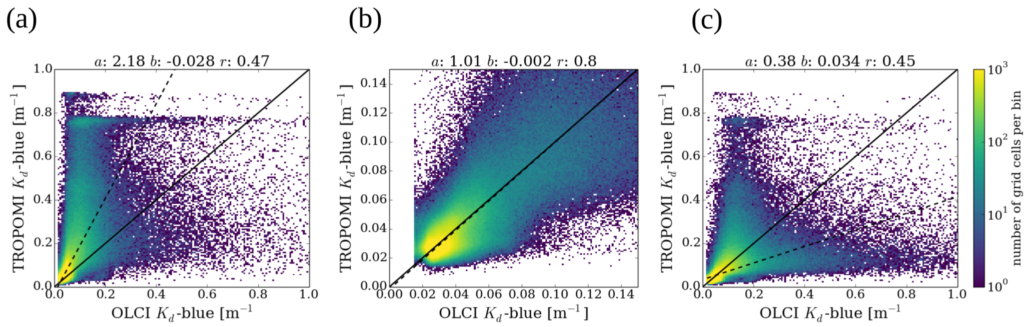

Figure 8: K_d-blue derived from a) original and offset corrected (b, c) TROPOMI VRS fit factors versus daily matchups of OLCI K_d-blue (for details on this products see S5POC-VR) for 11 May to 9 June 2018, both gridded at 0.083° for 11 May to 9 June 2018 and the Atlantic Ocean. Figure from Oelker *et al.* (2022b), suppl. material.

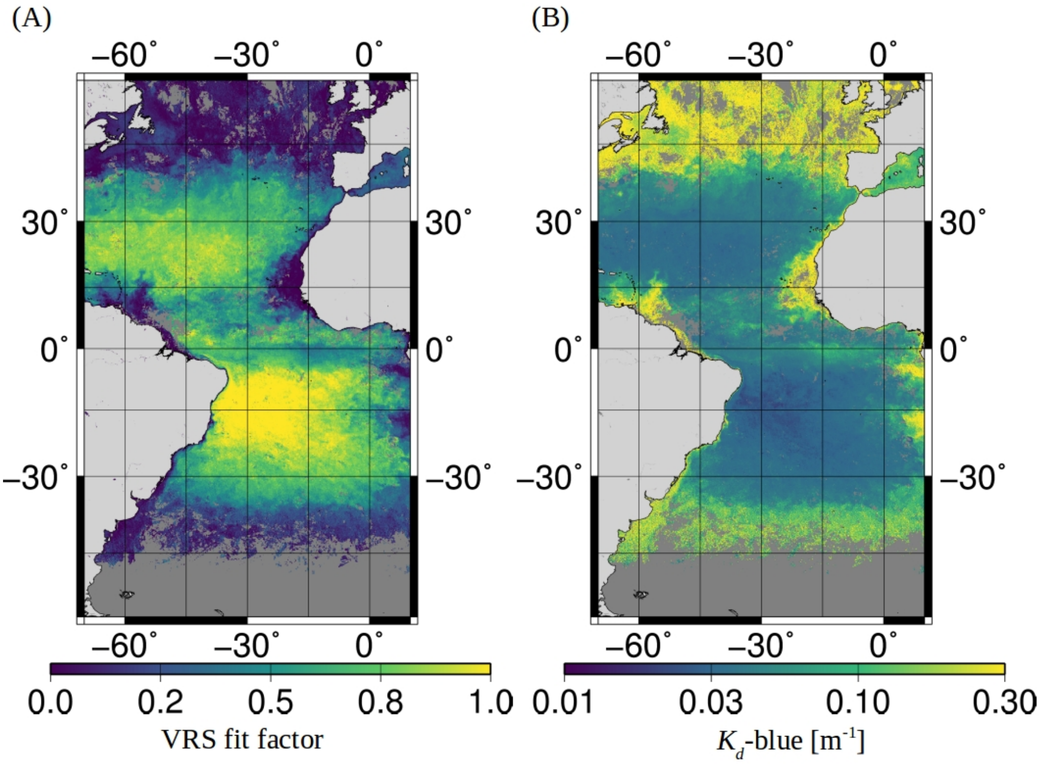

Figure 9: Original TROPOMI VRS fit factors (left) and correspondingly derived K_d-blue, both gridded at 0.083° as mean for 11 May to 9 June 2018 for the Atlantic Ocean. Figure from Oelker *et al.* (2022b), suppl. material.

Therefore, the offset correction applied to the input VRS-blue data for the

LUT was derived from comparing the low values (K_d <0.15 m^{-1}) of TROPOMI K_d-blue to those from the OLCI K_d-blue data set to determine the offset for VRS-blue that best corrects the data. This was based on considering daily 5 min gridded matchup K_d-blue data from TROPOMI and OLCI within the entire RV Polarstern expedition PS113 time period (11 May to 9 June 2018) and area of 50°S to 50°N and 70°W to 10°E. The offset correction was optimized such that a linear total-least square regression on this restricted comparison data set yielded a slope close to one. The optimal offset to VRS-blue fit factor was found to be 0.186. Regression statistics for using this setting to derive the final K_d-blue resulted in the comparison to OLCI K_d-blue in a slope of 1.01, an intercept of -0.002 m^{-1}, and a Pearson correlation coefficient of 0.80 (Figure 8b) for this restricted data set. The offset was used to correct all VRS fit factors, also retrieved for regions D, and by that the whole K_d-blue range (Figure 8c).

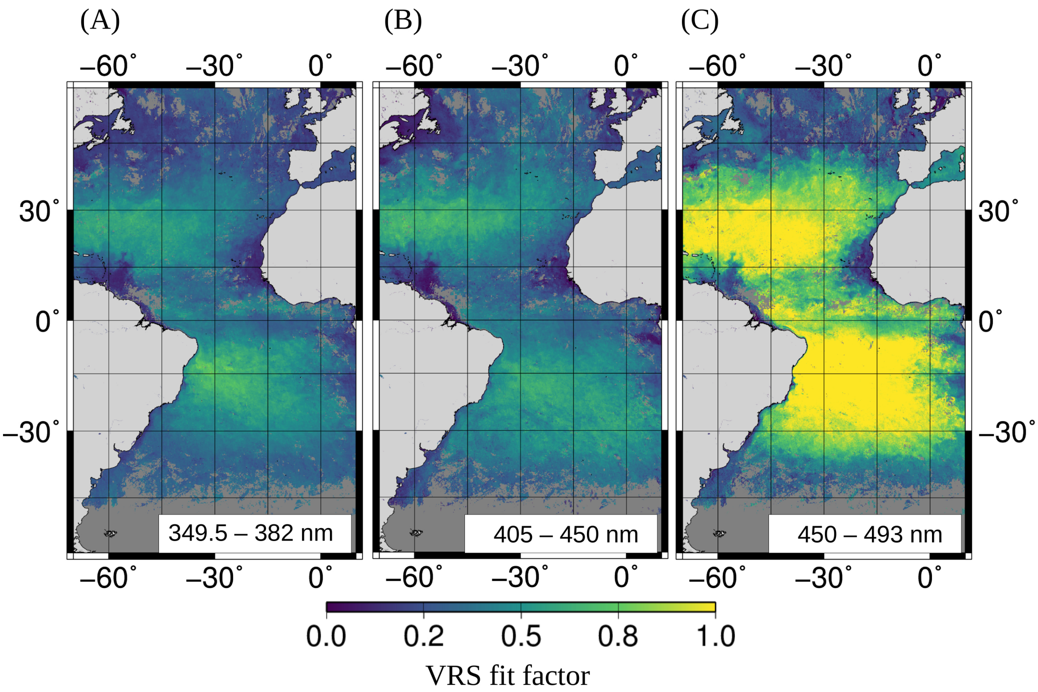

Figure 10: TROPOMI VRS fit factors in the (from left to right) UVA, short-blue and blue fit window in the Atlantic Ocean for 11 May to 9 Jun 2018. For TROPOMI VRS-blue fit factors an offset of 0.186 was added to the original VRS-blue (Figure 9). Figure from Oelker *et al.* (2022b).

Figure 10 shows VRS fit factors retrieved from TROPOMI level-1b data for the three PhytoDOAS fit windows in the UV, short-blue and blue for the same time period and area as described above. VRS-blue fit factors are offset corrected.

For all three fit windows, high and low VRS fit factors are found in typically low and high Chla corresponding to low and high light penetration into the ocean, respectively. As expected, the VRS signal increases with increasing wavelength window. The average root mean square (RMS) of all fit residuals in this area and time period and its standard deviation were evaluated to $1.0 \cdot 10^{3} \pm 3 \cdot 10^{-4}$ for the UV (excluding 26 outliers with RMS >4), $0.9 \cdot 10^{-3} \pm 2 \cdot 10^{-4}$ for the short-blue, and $1.0 \cdot 10^{3} \pm 3 \cdot 10^{-4}$ for the blue fit window. VRS fit factors from different fit windows are not strictly correlated, e.g., differences appear around Newfoundland and Great Britain.

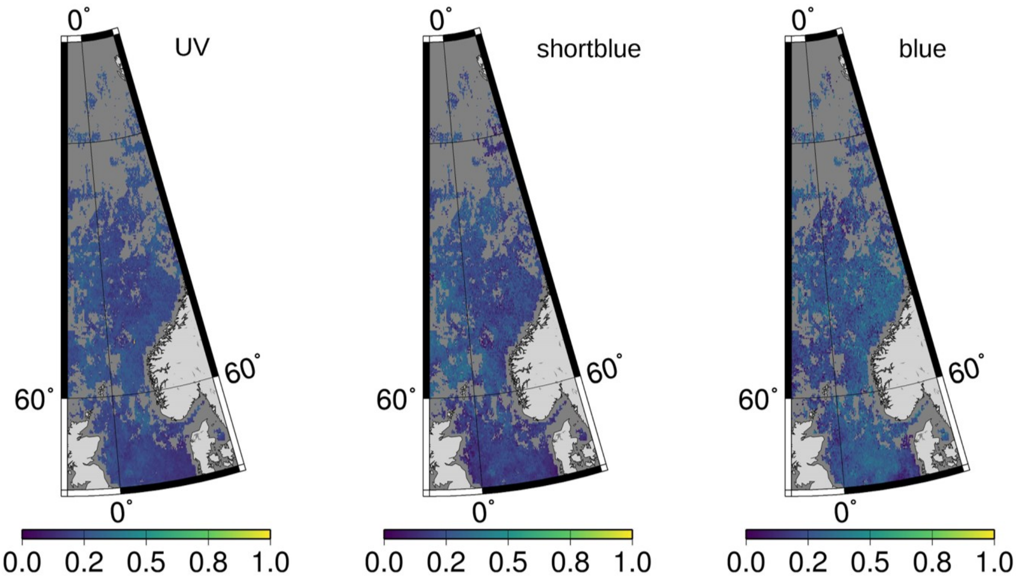

Figure 11: TROPOMI VRS fit factors (from left to right) UVA, short-blue and blue fit window for 11 Aug to 10 Sep 2019 for the North Sea up to the Fram Strait. For TROPOMI VRS-blue fit factors an offset of 0.186 was added. Pixels with SZA $>$ 70°were screened out, because 70° is the largest SZA in the LUT.

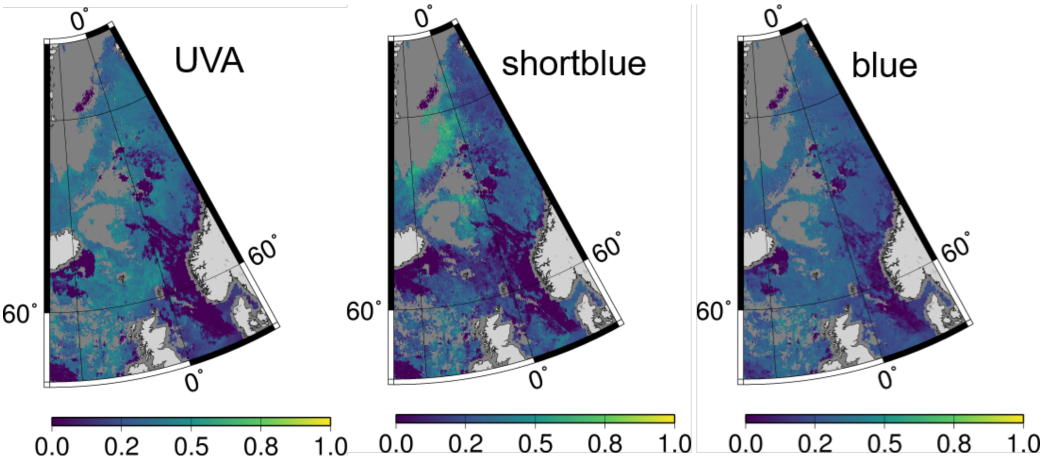

Figure 12: TROPOMI VRS fit factors (from left to right) UVA, short-blue and blue fit window for 27 Jun to 25 Jul 2020 for the North Sea up to the Fram Strait, including East Greenland waters. For TROPOMI VRS-blue fit factors, an offset of 0.186 was added. Pixels with SZA $>$ 70°were screened out, because 70° is the largest SZA in the LUT.

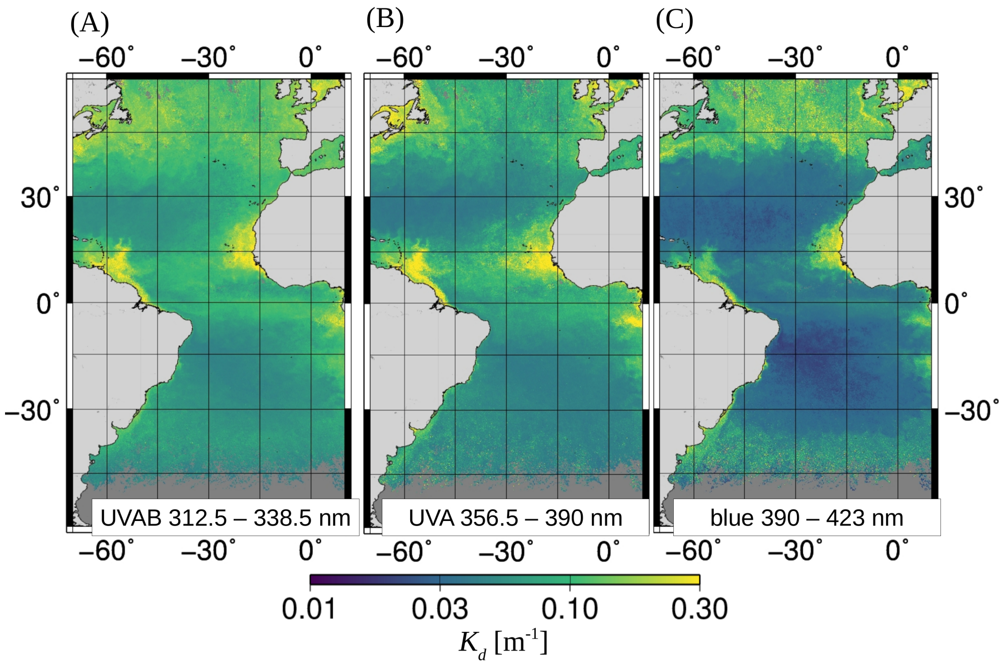

Figure 13: TROPOMI (A) K_d-UVAB, (B) K_d-UVA, and (C) K_d-blue gridded at 0.083° as mean for 11 May to 9 June 2018 for the Atlantic Ocean. Figure from Oelker *et al.* (2022b).

TROPOMI K_d was derived from the VRS fit factors, shown in Figure 10, Figure 11 and Figure 12, using the separate LUTs (as described in section 4.4.3) for each wavelength region. In Figure 13 the resulting (A) K_d-UVAB, (B) K_d-UVA, and (C) K_d-blue in the Atlantic Ocean for the PS113 (for region D, see Fig. 4 in S5POC-VR) can be seen for the same time period. Lowest K_d are found in the North and South Atlantic Gyres, highest K_d in the upwelling regions along the African coast and the Amazon river plume. With decreasing wavelength, K_d increases. However, K_d-UVAB is not generally larger than K_d-UVA. In upwelling regions off the coast of West Africa, the Amazon river plume, around Newfoundland, and around Great Britain, the ratio K_d-UVA/K_d-UVAB is larger than 1 (roughly 1.25 on average, 2 in extreme cases). Similarly in 2020 in the North Atlantic K_d-UVA is significantly higher even outcompeting K_d-blue. K_d-blue is much lower in the subtropical and tropical ocean and shows values between K_d-UVA and UVAB in the productive areas north of the North Atlantic Gyre.

5 Feasibility

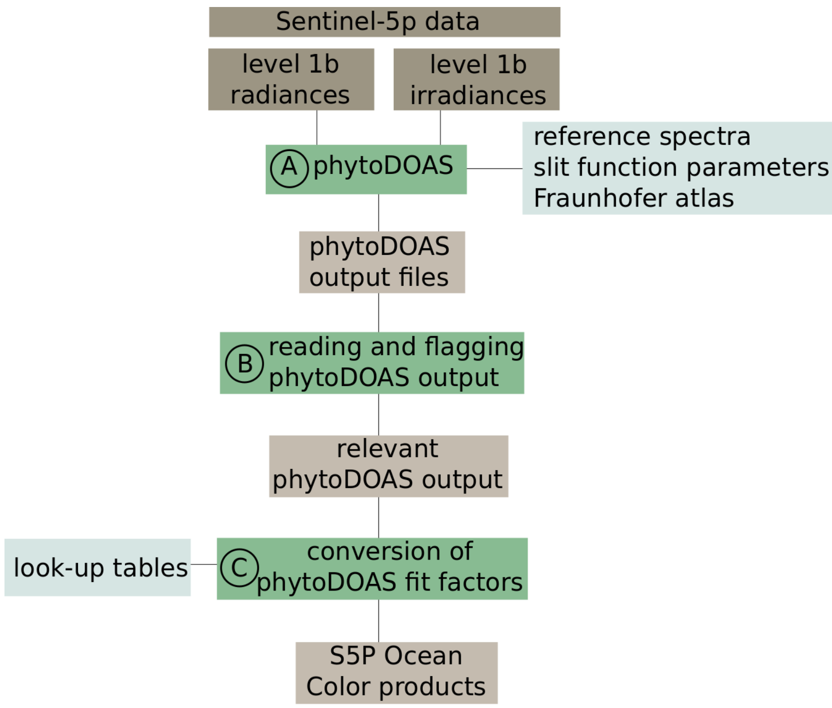

Figure 14: Scheme of the processing chain. Dynamic input files are shown in dark brown, intermediate and product files in light brown. Static input files are highlighted in grey. Processing steps A to C are shown in green.

Figure 14 schematically shows the processing chain of the TROPOMI ocean color retrievals. Dynamic input files are shown in dark grey, intermediate and output files in light grey, and static input files in light blue. The chain consists of three processing steps A, B, and C highlighted in green.

5.1 Computational effort

Processing one full orbit of TROPOMI data for all three targets of KD takes roughly 7.5 minutes for step A, 1 minute for step B, and 30 seconds for step C. Through introducing parallel computing on the super computer used, 200 orbits at the same time can be processed which enables to process a whole year for the three targets in less than 4 hours. In summary, the computational load of this product is low and the output file size similar to other S5P L2 products.

5.2 Input data

Retrieval processing of S5POC products requires dynamic and static input data.

5.2.1 Dynamic input

The main dynamic input data for the S5p OClO product are TROPOMI L1 products of band 3 (for KD-UVAB) and band 4 (for KD-UVA and KD-blue) radiance and irradiance. Global data is required. In addition to the TROPOMI lv1 data, TROPOMI NO2 OFFL data are used to extract cloud information which is added to the KD L2 files.

5.2.2 Static input

Static input data for the OClO retrieval have been briefly discussed in section 8 and include cross-sections and solar Fraunhofer atlas. They are available from the literature, cf. Table 8.2. In addition, the ISRF is required which is available from the S5p project.

5.3 Output Product Overview

Output data format follows the TROPOMI netcdf standard. Details on the product can be found in the S5POC PUM (Oelker *et al.*, 2022a).

6 Error analysis

Uncertainties associated with S5P ocean color products were assessed through the measurement fit errors (detailed in S5POC IAR, Bracher *et al.* (2022a)), the sensitivity analysis of S5POC retrievals using RTM (detailed in 6.1), intercomparison to ocean color products from multispectral satellite sensors and validation with in-situ data (both detailed in Bracher *et al.* (2022b)). Maximum errors obtained via the retrievals sensitivity studies are used as specific model errors and provided together with the measurement errors (fit errors) within the final error budget assessment (see Chapter 3 in S5POC IAR, Bracher *et al.* (2022a)). For S5POC K_d products their detailed and total uncertainties are also provided in the publication Oelker *et al.* (2022b).

6.1 Retrieval sensitivity

Here, we detail the results of the sensitivity analysis. Some of these results were obtained in previous studies related to similar atmospheric sensors used to obtain the same OC products (Dinter *et al.*, 2015; Wolanin *et al.*, 2015b; Oelker *et al.*, 2019). Settings in the RTM scenarios used for building the retrieval LUTs were investigated. It was tested how a change in a model parameter influences the resulting S5P ocean color product, e.g. the choice of chlorophyll-a absorption spectra in the UV region on the Kd-UVAB product. Also information on PhytoDOAS retrieval sensitivity from previous studies for estimating, e.g. the influence of the vertical distribution of Chl-a in the water column, is included here.

6.1.1 K_d algorithm sensitivity analysis

The algorithm sensitivity was extending the analysis by Oelker *et al.* (2019) which focused on aerosol and CDOM settings, to the parameters: CDOM slope, UV-absorbing pigments, liquid water absorption, wind speed, and ozone concentration. For each parameter, the sensitivity was analyzed as follows. An RTM simulation was performed to calculate radiances and radiant fluxes in which one parameter is increased or decreased with respect to the standard scenario used to build the LUT as described in section 4.4.3. The PhytoDOAS fit was performed on this modified scenario. Resulting VRS fit factors were converted to K_d using the LUT. The resulting K_d, K_d^{der}, was compared to the expected K_d, K_d^{exp}, calculated from the radiant fluxes of the modified scenario. The deviation of expected from derived K_d was determined as

$$\varepsilon \;=\; \frac{K_d^{\mathsf{exp}} - K_d^{\mathsf{der}}}{K_d^{\mathsf{exp}}}. \tag{5}$$

Since mainly only a change in inherent optical properties changes K_d, the parameters can be separated in two groups. One group comprises the atmospheric and surface parameters which have no or only a minimal effect on the mean K_d over the first optical depth, but may influence VRS since scattering is proportional to light intensity. The second group comprises the oceanic parameters which affect both, K_d and VRS. For the second group, K_d changes can be large, however, VRS changes accordingly, and K_d is retrieved correctly within an uncertainty which is only a fraction of the change in K_d.

In general, depending on observation geometry, a change of selected atmospheric or oceanic parameter can lead both to the increase and to the decrease of VRS signal (pseudo-absorption cross section). Taking into account that VRS signal is defined as

$$\sigma \;=\; \ln\frac{I^+}{I^-} \;=\; \ln\frac{I^- + \Delta I}{I^-} \;=\; \ln\left(1 + \frac{\Delta I}{I^-}\right)\;, \tag{6}$$

where I^+ and I^- are TOA radiances calculated including and excluding inelastic processes, respectively, $\Delta I = I^+ - I^-$ is the contribution of inelastic process. Accounting for that $\Delta I/I^-$ is significantly smaller than 1, we obtain for VRS signal the following approximation:

$$\sigma \;\approx\; \frac{\Delta I}{I^-}\,. \tag{7}$$

This approximation will be used in the following to explain the sign or magnitude of obtained K$_d$ deviations.

I: Atmospheric and surface parameters

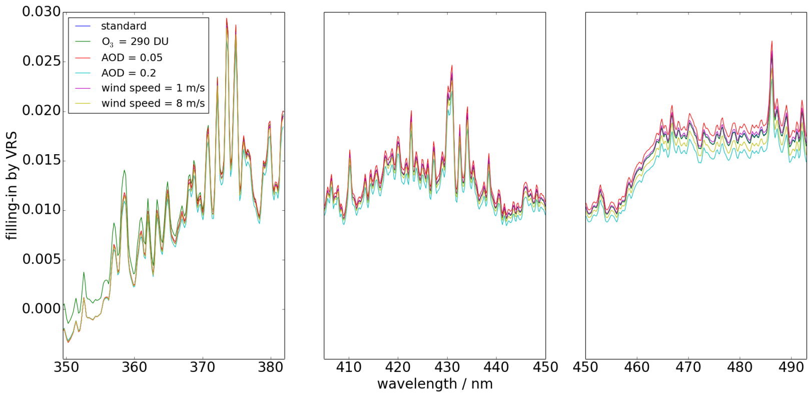

Figure 15: Filling-in by VRS for different model parameterizations in comparison to the standard simulation for the three wavelength ranges of the PhytoDOAS VRS fits. Figure from Oelker *et al.* (2022b), suppl. material.

Parameters within the first group were varied as follows: wind speed was reduced to 2 m/s and increased to 8 m/s (standard - 4.1 m/s); aerosol optical depth (AOD) was reduced to 0.05 and increased to 0.2 (standard - 0.1); ozone profile was changed to one with reduced total ozone column of 290 DU (standard - 420 DU). Figure 15 shows the influence of these selected atmospheric and surface parameters on the filling-in by VRS as determined by Equation (2) in section 4.2 for Chla of 0.1 mg/m^3. The influence of AOD and wind speed is largest for the blue fit window and decreases with decreasing wavelength. It is negligible for wavelengths smaller ∼360 nm. The influence of the ozone concentration is largest at the short wavelengths. It is negligible for wavelengths larger ∼370 nm.

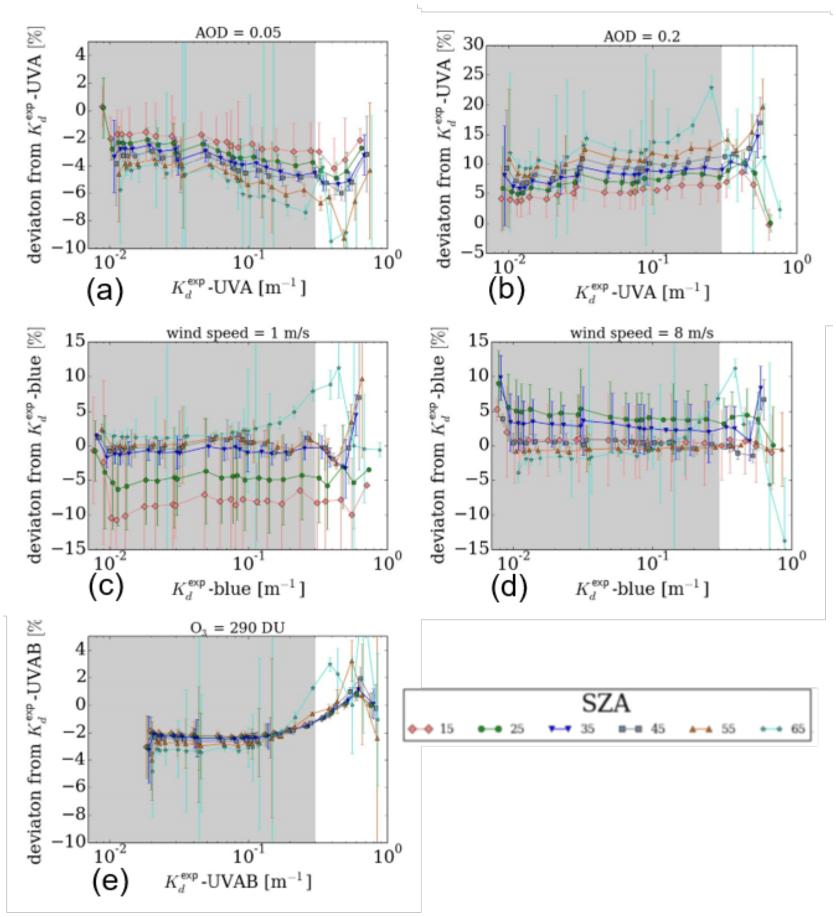

Figure 16: Deviation of derived from expected K_d in case of (a) reduced AOD, (b) increased AOD, (c) reduced wind speed, (d) increased wind speed, and (e) reduced ozone column for different SZA. Results were averaged for different VZA with the standard deviation given as error bar. (a), (b) show results for K_d-UVA, (c), (d) for K_d-blue, and (e) for K_d-UVAB. Figure from Oelker *et al.* (2022b).

Ia: Aerosol

The deviations of derived from expected K_d caused by the variation of AOD are presented in Figs. 17 and Figs. 18 in the case of 50% reduced and 50% enhanced AOD, respectively.

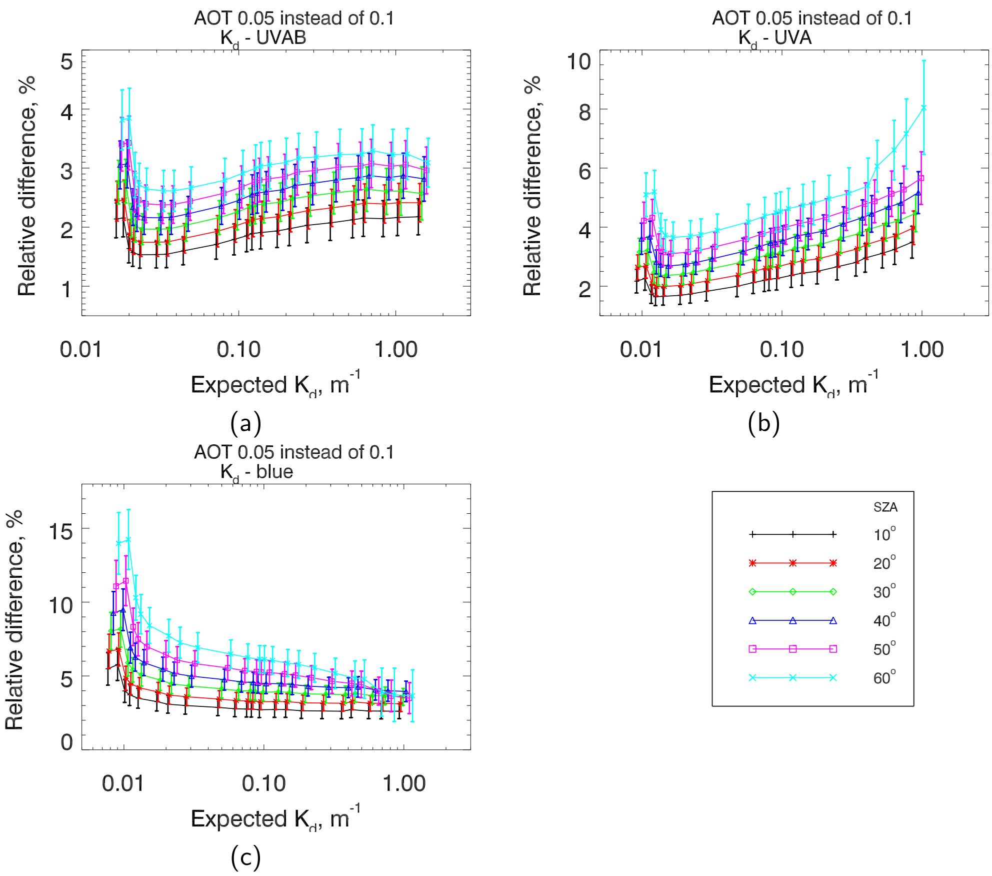

Figure 17: Deviation of derived from expected K$_d$ in the case of 50% reduced AOD. (a) K$_d$-UVAB, (b) K$_d$-UVA, (c) K$_d$-blue. Results were averaged for different zenith and azimuth angles with the standard deviation given as errorbar

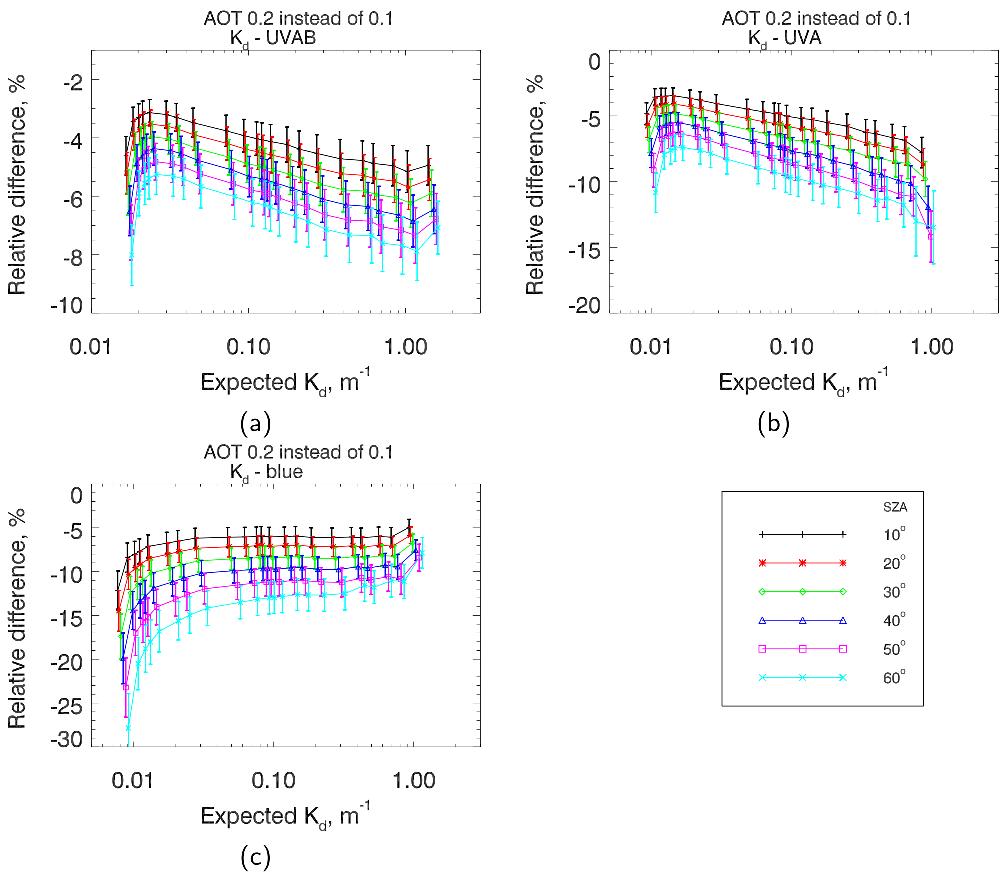

Figure 18: Deviation of derived from expected K$_d$ in the case of 50% enhanced AOD. (a) K$_d$-UVAB, (b) K$_d$-UVA, (c) K$_d$-blue. Results were averaged for different zenith and azimuth angles with the standard deviation given as errorbar

The decrease of AOD leads to the increase of VRS fit factors and therefore to the decrease of K$_d$ and vice versa in the case of increase AOD. As results one can see in Figs. 17 positive deviations of retrieved K$_d$ whereas Figs. 18 show negative ones. The impact of aerosol variations on the derivation of K$_d$, increased with the increase of the wavelength. In particular, the relative deviations are in the range 1%-4%, 2%-8%, and 2%-15% in the case of K$_d$-UVAB, K$_d$-UVA, and K$_d$-blue, respectively. In the case of 50% enhanced AOD the magnitude of deviations are similar but they are negative. One can also see that the magnitude of deviations depends on the SZA and increased with the increasing of solar angle.

LUTs for errors caused by variation of aerosol optical thickness

The deviations of derived from expected K$_d$ caused by the variation of AOD are

summarized in LUTs "Err_lut_W1.atm", "Err_lut_W2.atm", and "Err_lut_W3.atm" for "UVAB", "UVA", and "short-blue", respectively.
Columns 6 and 7 in these files contain the relative errors [%] caused by usage of AOT equal to $\tau_- = 0.05$ and $\tau_+ = 0.2$, respectively, in contrast to AOT 0.1 used in main LUTs for K_d. The results from these columns enable to estimate the error caused by AOT if this AOT is known for a selected measurement point. Indeed, let us define $\tau_{lut} = 0.1$ as used in main LUTs, than under assumption of linear dependence between error of K_d estimation and AOT, we have in the case of $\tau > \tau_{lut}$:

$$\varepsilon(\tau) = \varepsilon_{lut}(\tau_+)\,\frac{\tau - \tau_{lut}}{\tau_+ - \tau_{lut}}\ , \tag{8}$$

and in the case of $\tau < \tau_{lut}$:

$$\varepsilon(\tau) = \varepsilon_{lut}(\tau_-)\,\frac{\tau_{lut} - \tau}{\tau_{lut} - \tau_-}\ . \tag{9}$$

Taking into account that $\tau_- = \tau_{lut}/2$ and $\tau_+ = 2\,\tau_{lut}$, we have

$$\varepsilon(\tau) = \varepsilon_{lut}(2\tau_{lut})\,\frac{\tau - \tau_{lut}}{\tau_{lut}}\ , \quad \tau > \tau_{lut}\ , \tag{10}$$

$$\varepsilon(\tau) = 2\,\varepsilon_{lut}(\tau_{lut}/2)\,\frac{\tau_{lut} - \tau}{\tau_{lut}}\ , \quad \tau < \tau_{lut}\ . \tag{11}$$

We note that $\varepsilon_{lut}(2\tau_{lut})$ and $\varepsilon_{lut}(\tau_{lut}/2)$ for a selected observation / illumination geometry and the retrieved VRS scaling factor can be obtained by the same way as in the case of K_d using the main LUTs.
In the absence of an additional information about AOT the error caused by AOT will be estimated as $max(|\varepsilon_{lut}(2\tau_{lut})|, |\varepsilon_{lut}(\tau_{lut}/2)|)$.

Ib: Wind speed

Depending on observation geometry, a change of Wind Speed (WS) magnitude can lead both to the increase and to the decrease of VRS signal. Accounting for that the decrease of wind speed leads to the increase of I^- in glint directions, one can see that according to Eq. (7) this results in the decrease of σ. In order to compensate the decrease of σ the VRS fit factor of PhytoDOAS fit needs to be also decreased. (Let us recall that in PhytoDOAS fit the constant pseudo-absorption cross section corresponding to WS=4.1 m/s is used.) In turn the decrease of VRS fit factor results in the increase of K_d derived using LUTs. Following Eq. (5), we expect negative deviations derived from expected K_d in the glint range by the decrease of wind speed.
The deviations of derived from expected K_d caused by the variation of wind speed

are presented in Figs. 19 and Figs. 20 in the case of ∼50% reduced (2 m/s) and ∼50% enhanced (8 m/s) WS, respectively, as compare to 4.1 m/s used for LUTs.

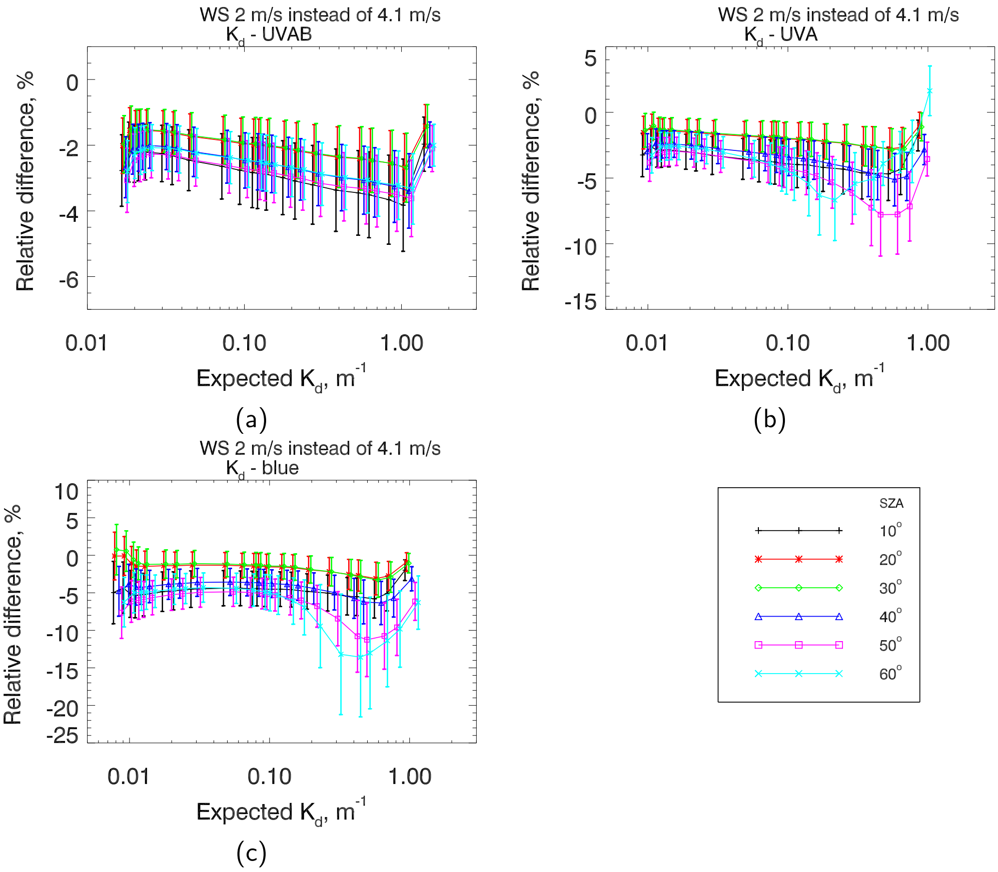

Figure 19: Deviation of derived from expected K_d in the case of reduced WS. (a) K_d-UVAB, (b) K_d-UVA, (c) K_d-blue. Results were averaged for different zenith and azimuth angles with the standard deviation given as errorbar

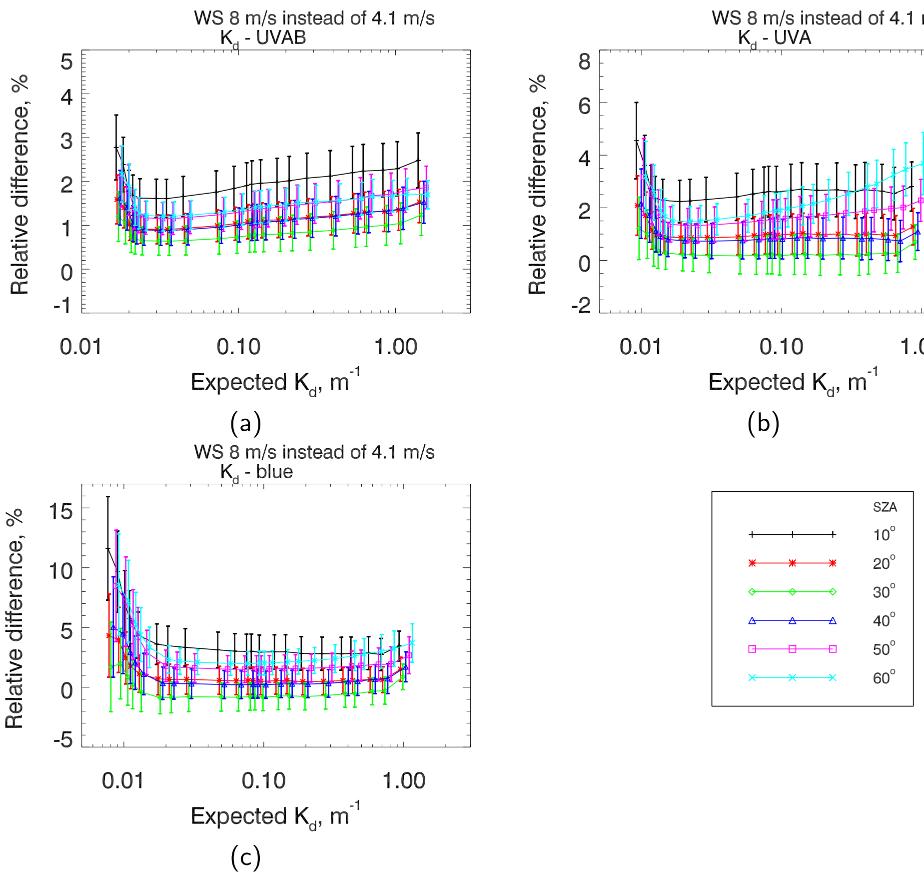

Figure 20: Deviation of derived from expected K$_d$ in the case of enhanced WS. (a) K$_d$-UVAB, (b) K$_d$-UVA, (c) K$_d$-blue. Results were averaged for different zenith and azimuth angles with the standard deviation given as errorbar

One can see from these plots that in general the decrease of WS leads to the decrease of averaged VRS fit factors and therefore to the increase of derived K$_d$ and vice versa in the case of increased WS. As results one can see in Fig. 19 negative deviations of retrieved K$_d$ whereas Fig. 20 show positive ones. In particular, the maximal relative deviations (after averaging over zenith and azimuth angles) in the case of reduced WS are -4%, -8%, and -15% for K$_d$-UVAB, K$_d$-UVA, and K$_d$-blue, respectively. It is worth to notice that the maximal contribution in deviations bring observation directions in the glint range corresponding to the zero azimuth angle. Excluding these observation directions, one can reduce maximal relative deviations especially in the case of K$_d$-blue. In particular, the maximal relative deviations in this case are -3%, -5%, and -5% in the case of K$_d$-UVAB, K$_d$-UVA, and K$_d$-blue, respectively.
The maximal relative deviations in the case of increased WS (8 m/s) are positive

and equal to 3%, 4%, and 10% for K$_d$-UVAB, K$_d$-UVA, and K$_d$-blue, respectively. In contrast to the decreased WS the excluding of observations in glint direction does not significantly reduce obtained deviations.

LUTs for errors caused by variation of wind speed

The deviations of derived from expected K$_d$ caused by the variation of wind speed (v) are presented in LUTs "Err_lut_W1.atm", "Err_lut_W2.atm", and "Err_lut_W3.atm" for "UVAB", "UVA", and "short-blue", respectively. Columns 8 and 9 in these files contain the relative errors [%] caused by the usage v equal to $v_- = 2\,m/s$ and $v_+ = 8\,m/s$, respectively, in contrast to $v = 4.1\,m/s$ used in the main LUTs for K_d. The results of these columns enable us to estimate the error caused by the wind speed if this v is known for a selected measurement point.
Let us define $v_{lut} = 4.1$ as used in main LUTs, than under assumption of linear dependence between error of K_d estimation and wind speed, we have in the case of $v > v_{lut}$:

$$\varepsilon(v) = \varepsilon_{lut}(v_+)\,\frac{v - v_{lut}}{v_+ - v_{lut}}\ , \tag{12}$$

and in the case of $v < v_{lut}$:

$$\varepsilon(v) = \varepsilon_{lut}(v_-)\,\frac{v_{lut} - v}{v_{lut} - v_-}\ . \tag{13}$$

We note that $\varepsilon_{lut}(v_-)$ and $\varepsilon_{lut}(v_+)$ for the selected observation / illumination geometry and the retrieved VRS scaling factor can be obtained in the same way as in the case of K_d using the main LUTs.
In the absence of an additional information about WS the error caused by wind speed will be estimated as $max(|\varepsilon_{lut}(v_-)|, |\varepsilon_{lut}(v_+)|)$.

Ic: Ozone concentration

The decrease of ozone vertical column leeds in general to the decrease of radiation absorption in the atmosphere and in turn to the increase of radiation which reaches ocean surface, especially in the UV spectral range. On one hand this results in the increase of energy transform from short wavelengths to the long ones caused by the vibrational Raman scattering. On the another hand the decrease of absorption in the atmosphere leads to the increase of outgoing radiation at top of atmosphere. According to Eq. (7), the increase of ΔI and increase of I^- can partly compensate each other. However, taking in the account that in the spectral range 280 - 350 mm the ozone absorption decreases with the increase of wavelength, one can expect that the increase of ΔI has more impact on σ then the increase of I^- and it is reasonable to expect the enhance of σ by the reduce

of ozone vertical column. In order to compensate the increase of σ the VRS fit factor of PhytoDOAS fit needs to be also increased to compensate pseudo-absorption cross section corresponding to 430 DU used for LUTs. The increase of VRS fit factor results in the decrease of K$_d$ derived using LUTs. Following Eq. (5), we expect positive deviations derived from expected K$_d$ in the case of decrease of ozone column.
The deviations of derived from expected K$_d$-UVAB caused by the variation of ozone column is presented in Fig. 21 in the case of ~33% reduced (290 DU) as compare to 430 DU used for LUTs.

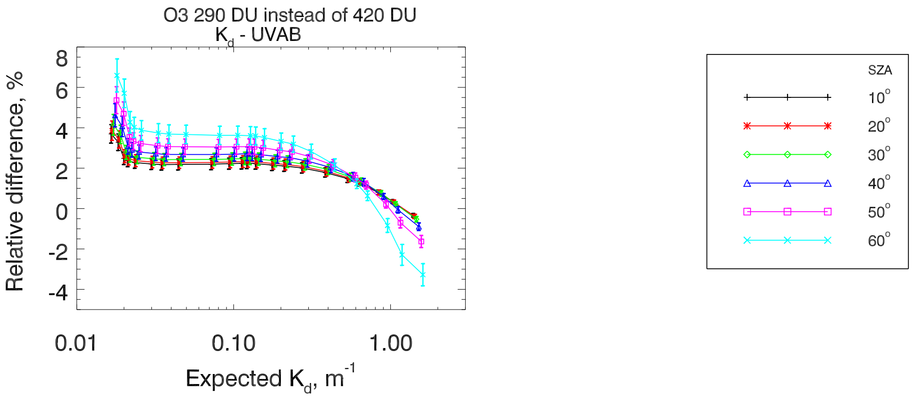

(a)

Figure 21: Deviation of derived from expected K$_d$-UVAB in the case of reduced ozone vertical column (290 DU instead of 430 DU used for LUTs). Results were averaged for different zenith and azimuth angles with the standard deviation given as errorbar.

One can see from Fig. 21 that maximal deviations reach 4%-6% depending on the solar zenith angle in the case of minimal values of expected K$_d$-UVAB. The deviations are positive what confirms above considerations.
The impact of ozone vertical column variations on the K$_d$-UVA and K$_d$-blue is neglectable and not shown here.

LUTs for errors caused by variation of the ozon vertical column

The deviations derived from expected K$_d$ caused by the variation of the ozone column (q) are presented in LUT "Err_lut_W1.atm".
Column 10 in this file contains the relative errors [%] caused by usage q equal to $q_- = 290\,DU$ in contrast to $q = 420\,DU$ used in main LUTs for K_d. The results from this column enable to estimate the error caused by the ozone column if this q is known for a selected measurement point.

Let us define $v_{lut} = 420\,DU$ as used in main LUTs, than under assumption of linear dependence between error of K_d estimation and ozone column, we have in the case of $q < q_{lut}$:

$$\varepsilon(q) = \varepsilon_{lut}(q_-)\,\frac{q_{lut} - q}{v_{lut} - q_-}\ . \tag{14}$$

We note that $\varepsilon_{lut}(q_-)$ for the selected observation/illumination geometry and the retrieved VRS scaling factor can be obtained in the same manner as in the case of K_d using the main LUTs.
In the absence of an additional information about ozone column the error caused by q will be estimated as $|\varepsilon_{lut}(q_-)|$.

Later on, results will show that TROPOMI K_d can not be well retrieved for scenes with $K_d >$ 0.3 or 0.5 m^{-1} within S5POC regions C and D, respectively, discussed in S5POC VR. Also, the retrieval is less robust at high SZA and at high VZA, which causes large error bars in the plots. This effect should be kept in mind, when the algorithm is applied in high latitudes. In the investigated Atlantic region, SZA are only moderately high and satellite pixels with high VZA are often screened out by the cloud filter due to their larger pixel size.

In summary, the influence of atmospheric and surface parameterizations is generally low on the K_d retrievals. Uncertainties increase with the difference between conditions found for an actual satellite scene and the average ones used in the simulated standard scenario. Largest uncertainties can be expected for scenes with high aerosol loading, which only occur in specific regions and times of the year (Remer *et al.*, 2008). For the Atlantic region, Saharan dust storms can have a significant influence (e.g., van der Does *et al.*, 2016). Maritime aerosols were investigated here, terrestrial dust might have even stronger impacts. These critical scenes are largely removed through the strict cloud filter criterion used in this study (cloud fraction of 0.01). In the future, the dimensions of the LUT can be increased, when confidence in performance of K_d retrievals has been gained by comparison with larger in-situ data sets than available for this study. The total ozone column, AOD, and wind speed can be included in the LUT and taken from ancillary data (some variables also available from TROPOMI) to further reduce uncertainty in TROPOMI K_d data sets.

II Oceanic parameters

The case-1 assumption is generally not valid in the UV domain. The absorption coefficient can not be accurately described using Chla (Vasilkov *et al.*, 2002; Morel *et al.*, 2007). The influence of the case-1 parameterization used for the optical constituents in the ocean on the ultraviolet K_d retrievals needs to be checked carefully. As introduced in section 4.3, the case-1 parameterization for the visible wavelength range was used in combination with a recent pure water absorption spectrum accurately measured for UV wavelengths Mason *et al.* (2016). Nevertheless, the influence of the choice of water absorption spectrum was assessed. A modified scenario was simulated with liquid water absorption coefficients from Pope & Fry (1997) which significantly differ at short wavelengths from those measured by Mason *et al.* (2016), see Oelker (2021).

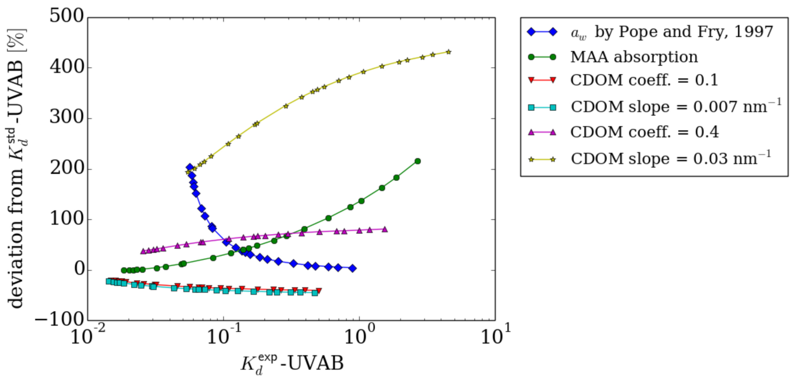

Figure 22: Deviation of K_d^{exp}-UVAB as in the modified scenario from K_d-UVAB in the standard scenario as function of K_d^{exp}-UVAB for tested variations in oceanic parameter. Figure from Oelker *et al.* (2022b).

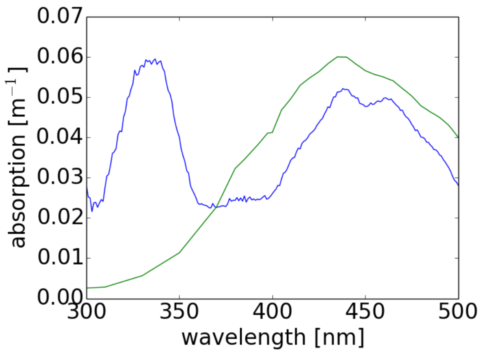

Figure 23: Phytoplankton absorption at Chla of 1 mg/m^3 in the standard (green) and in the modified (blue) simulations (S9 from Bracher & Wiencke, 2000).

High uncertainty also lies within the settings for phytoplankton and CDOM absorption. Presence of mycosporine amino acids (MAA) causes higher UV absorption than prescribed in the standard case-1 parameterization. MAA absorb between 320 and 350 nm with a peak around 330 to 340 nm (Vernet *et al.*, 1994; Bracher & Wiencke, 2000). Presence of these UV-absorbing pigments should therefore mainly influence K_d-UVAB (Wang *et al.*, 2021). In the study by Bracher & Wiencke (2000) different phytoplankton communities had been sampled in the Southern Ocean. We have further analysed these data by normalizing them to chl-a concentration. The results show that within similar phytoplankton communities the specific absorption can vary by a factor 5.2 in the UV. A modified scenario was simulated using a phytoplankton absorption spectrum with medium MAA absorption (S9 from Bracher & Wiencke (2000), see Figure 23). High variability can also be expected for the CDOM slope, 0.01 to 0.03 nm^{-1} (Vodacek *et al.*, 1997) as compared to 0.014 nm^{-1} in the standard case-1 scenario. Modified RTM simulations were made with a reduced CDOM slope of 0.011 nm^{-1} and an increased CDOM slope of 0.0194 nm^{-1}. Also the CDOM absorption coefficient was increased and decreased two times, while keeping the CDOM slope as constant equal to 0.0164 nm^{-1}.

IIa Magnitude of CDOM absorption coefficient

The deviations of derived from expected K_d caused by the variation of CDOM absorption coefficient magnitude are presented in Fig. 24 and Fig. 25 in the case of two times increased and two times decreased absorption coefficient, respectively.

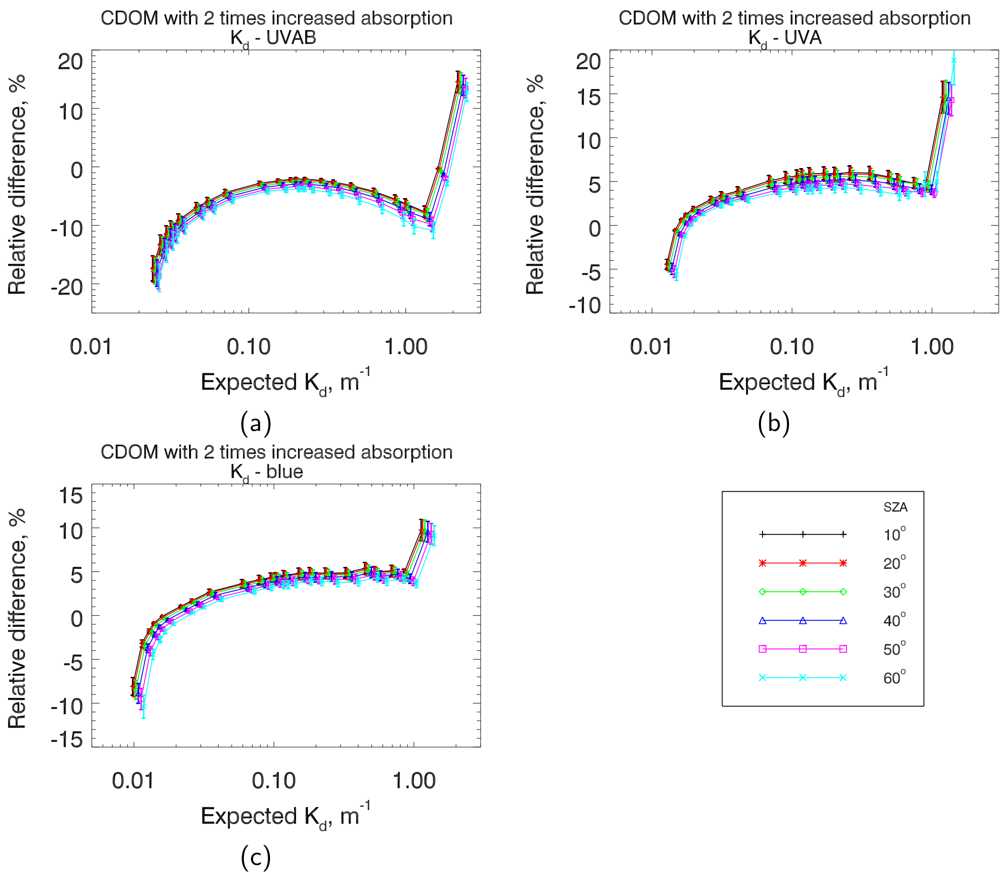

Figure 24: Deviation of derived from expected K_d in the case of two times increased CDOM absorption coefficient. (a) K_d-UVAB, (b) K_d-UVA, (c) K_d-blue. Results were averaged for different zenith and azimuth angles with the standard deviation given as errorbar.

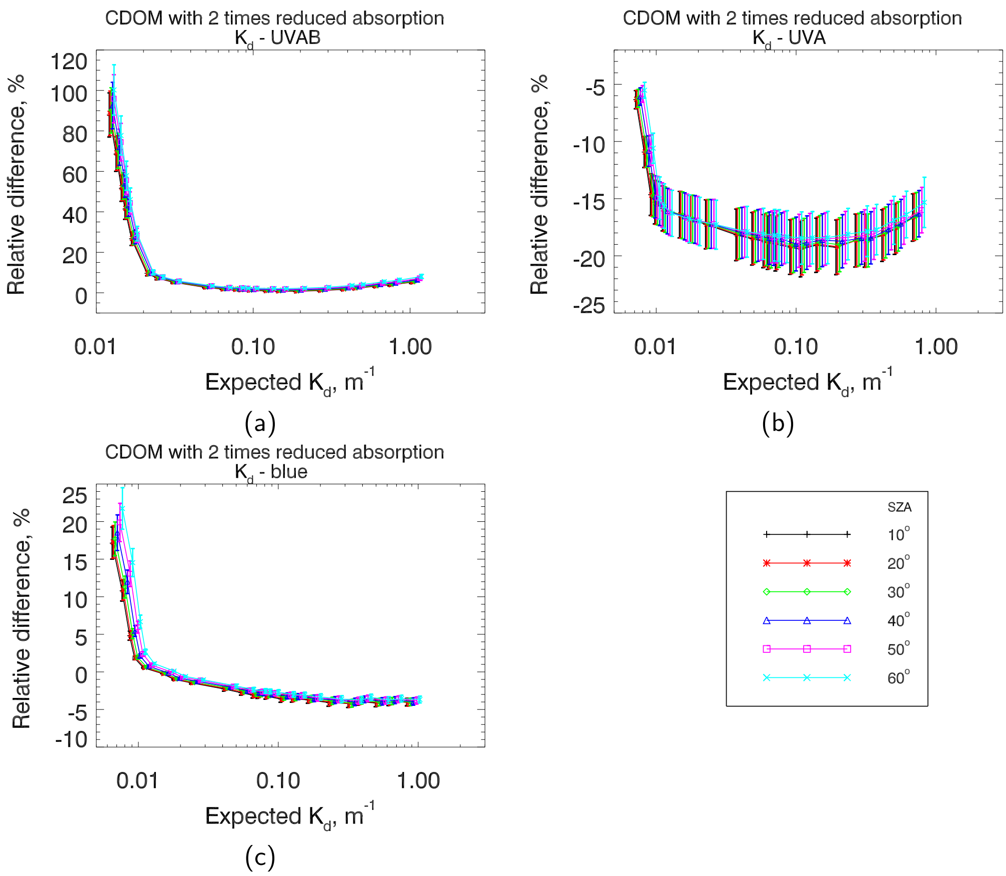

Figure 25: Deviation of derived from expected K$_d$ in the case of two times reduced CDOM absorption coefficient. (a) K$_d$-UVAB, (b) K$_d$-UVA, (c) K$_d$-blue. Results were averaged for different zenith and azimuth angles with the standard deviation given as errorbar.

In order to understand obtained deviations we use the following approximation for VRS signal (pseudo-absorption cross section) derived above, namely

$$\sigma \approx \frac{\Delta I}{I^-}, \quad (15)$$

where ΔI is a contribution of inelastic process, I^- is the TOA radiance calculated excluding inelastic process.
Taking into account that increasing of CDOM absorption leads to the decrease of both ΔI and I^-, one can expect both negative and positive signs of ε. The results presented in Fig. 24 in the case of two times increased absorption coefficient confirm this assumption. In the case of two times decreased absorption coefficient (see Fig. 25) one can see positive deviations for K$_d$-UVAB and negative ones for

K$_d$-UVA at all expected values of K$_d$. This demonstrate that in the forme case effect of increasing ΔI is weaker than effect of increasing I^-. In the later case vice versa.

IIb Sensitivity with respect to slope of CDOM absorption coefficient The deviations of derived from expected K$_d$ caused by the variation of CDOM absorption coefficient slope are presented in Fig. 26 and Fig. 27 in the case of the slope equal to 0.0194 nm^{-1} and to 0.011 nm^{-1}, respectively, which correspond to the representation of CDOM absorption as absorption by pure fulvic or by pure humic acid.

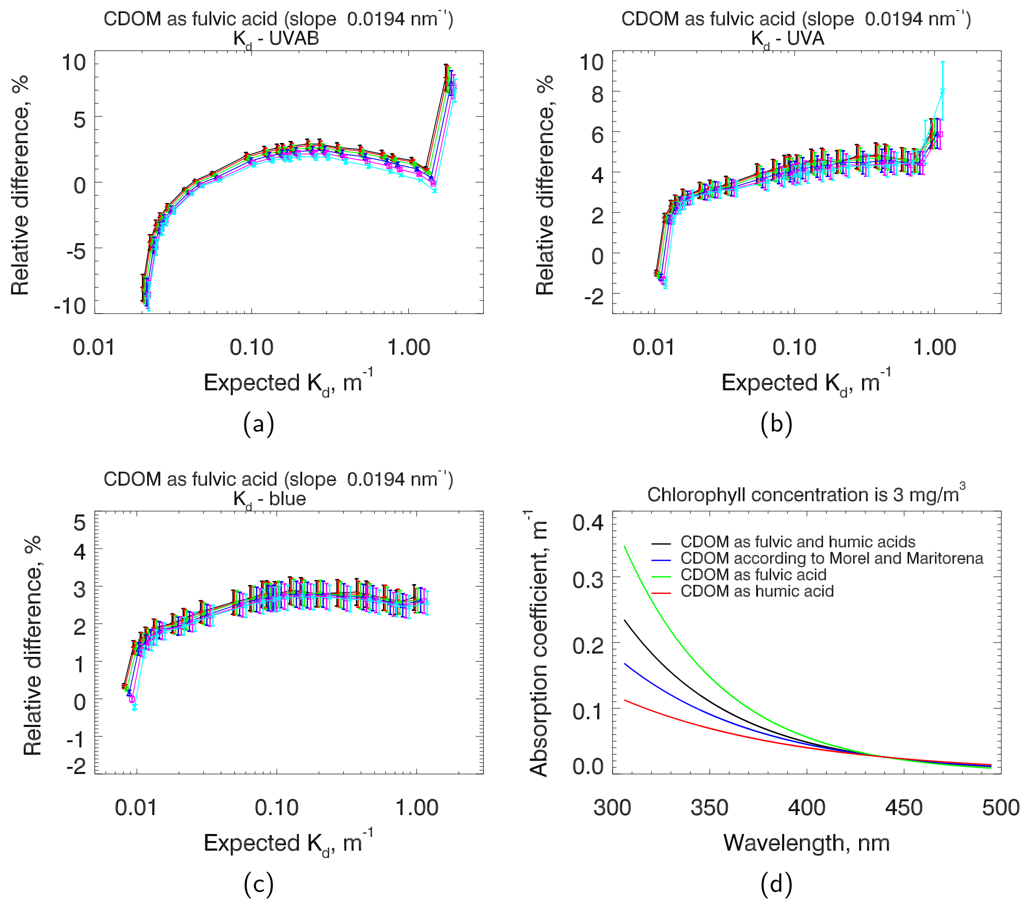

Figure 26: Deviation of derived from expected K$_d$ in the case of slope 0.0194 nm^{-1}. (a) K$_d$-UVAB, (b) K$_d$-UVA, (c) K$_d$-blue. Results were averaged for different zenith and azimuth angles with the standard deviation given as errorbar.

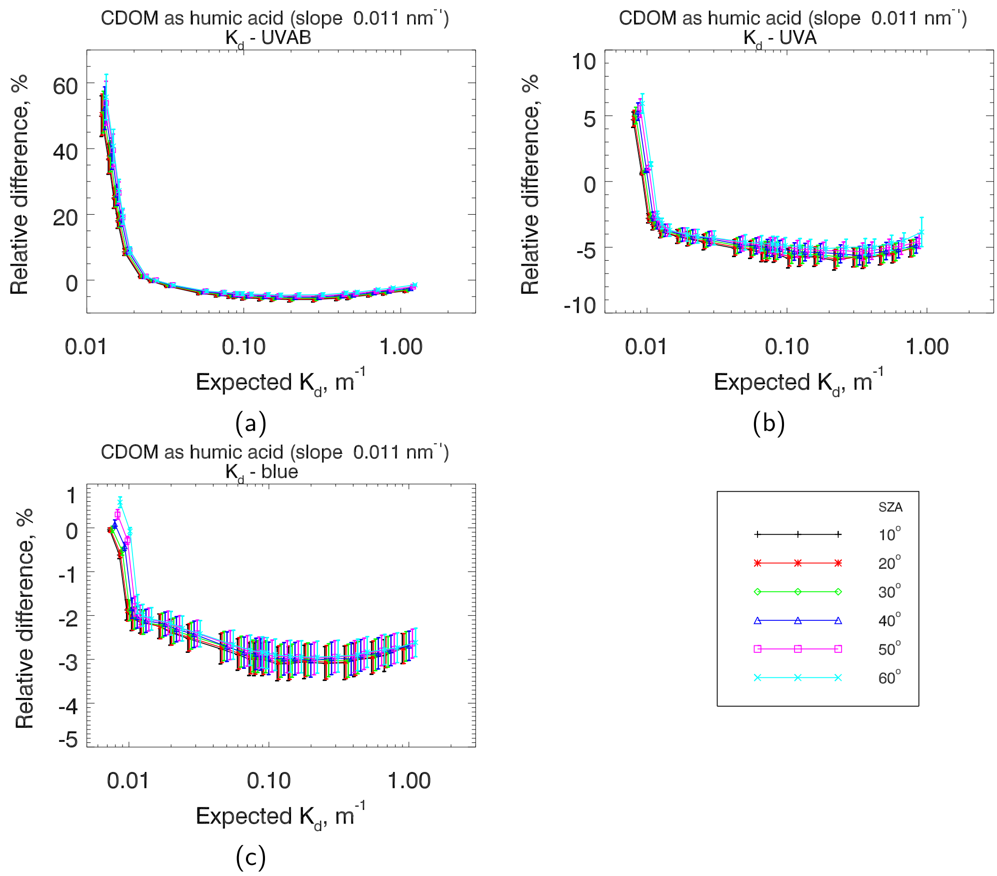

Figure 27: Deviation of derived from expected K$_d$ in the case of slope 0.011 nm^{-1}. (a) K$_d$-UVAB, (b) K$_d$-UVA, (c) K$_d$-blue. Results were averaged for different zenith and azimuth angles with the standard deviation given as errorbar.

The deviations of derived from expected K$_d$ in the case of CDOM absorption coefficient according to (Morel & Maritorena, 2001) are presented in Fig. 28.

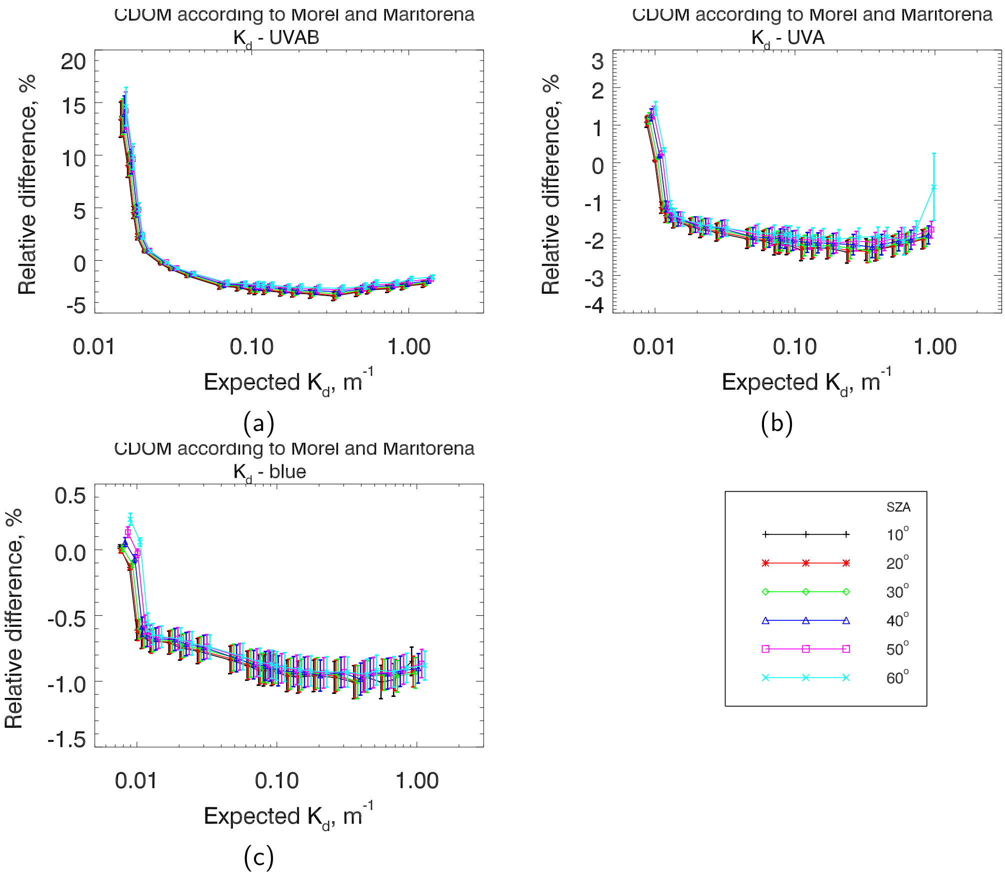

Figure 28: Deviation of derived from expected K_d in the case of CDOM absorption coefficient according to (Morel & Maritorena, 2001). (a) K_d-UVAB, (b) K_d-UVA, (c) K_d-blue. Results were averaged for different zenith and azimuth angles with the standard deviation given as errorbar.

The lower right panel of Fig. 26 demonstrates the wavelength dependent CDOM absorption coefficients corresponding to $3\,\mathrm{mg/m^3}$ chlorophyll concentration.
As can be seen from comparison of results presented in Fig. 27 and Fig. 25, the decrease of slope leads to the similar effect as a decrease of absorption coefficient. Similar to that the comparison of results presented in Fig. 26 and Fig. 24 shows that the increase of slope leads to the comparable effect as a increase of absorption coefficient. However, in both cases the magnitude of ε is smaller as expected in the case of slope variations.

In the former version of this retrieval, the sensitivity to the pure sea water spectrum has been investigated (Oelker *et al.* (2022b)). The change of using the old water spectrum by Pope & Fry (1997) compare to the new on by Mason *et al.* (2016) results in an overestimation of 15% for clear water scenarios which reduces to zero for high Chla scenarios. The overestimation is counter-intuitive, since K_d^{exp} is higher than K_d^{std}. A changed parameterization often also causes a spectral change in K_d which impacts the VRS fit quality and can result in this unexpected behavior.

In conclusion, the K_d-UV retrievals are rather insensitive to the chosen RTM parameterization compared to the large variability that this parameterization causes in K_d in the ultraviolet spectral range.

LUTs for oceanic parameters

In the framework of the sensitivity study we considered the deviations of the derived from the expected K_d caused by the variation of

- 1 - CDOM absorption coefficient magnitude in the case of two times increased absorption coefficient;
- 2 - CDOM absorption coefficient magnitude in the case of two times decreased absorption coefficient;
- 3 - CDOM absorption coefficient according to Morel and Maritorena (2001);
- 4 - CDOM absorption coefficient slope in the case of the slope equal to 0.0194 nm^{-1}, which correspond to the representation of CDOM absorption as absorption by pure fulvic acid;
- 5 - CDOM absorption coefficient slope in the case of the slope equal to 0.011 nm^{-1}, which corresponds to the representation of CDOM absorption as absorption by pure humic acid.

For each observation/illumination geometry the relative error was calculated according to Eq. (5). Taking into account that the relative errors demonstrate dependence on the selected geometry and VRS scaling factor, we have prepared the LUT containing RMS error for all considered above variations of the CDOM absorption coefficient calculated as

$$\epsilon = \sqrt{\frac{1}{N}\sum_{i=1}^{N}\varepsilon_i^2}\,, \tag{16}$$

where $N = 5$ in the case under consideration.
The obtained results for ϵ are presented in LUTs "RMS_lut_W1.oce", "RMS_lut_W2.oce", and "RMS_lut_W3.oce" for "UVAB", "UVA", and "short-blue" windows, respectively. The value of ϵ for selected observation/illumination

geometry and retrieved VRS scaling factor can be obtained using interpolation technique by the same manner as in the case of K_d using the main LUTs.

To demonstrate results summarized in RMS errors LUTs let us consider figures 29 - 31. These figures show RMS errors of K_d UVAB, UVA, and short-blue, respectively, for all viewing and solar angles (except of solar zenith angle 70°) and four selected concentrations of chlorophyll: 20 mg/m^3, 8 mg/m^3, 0.7 mg/m^3 and 0.003 mg/m^3.

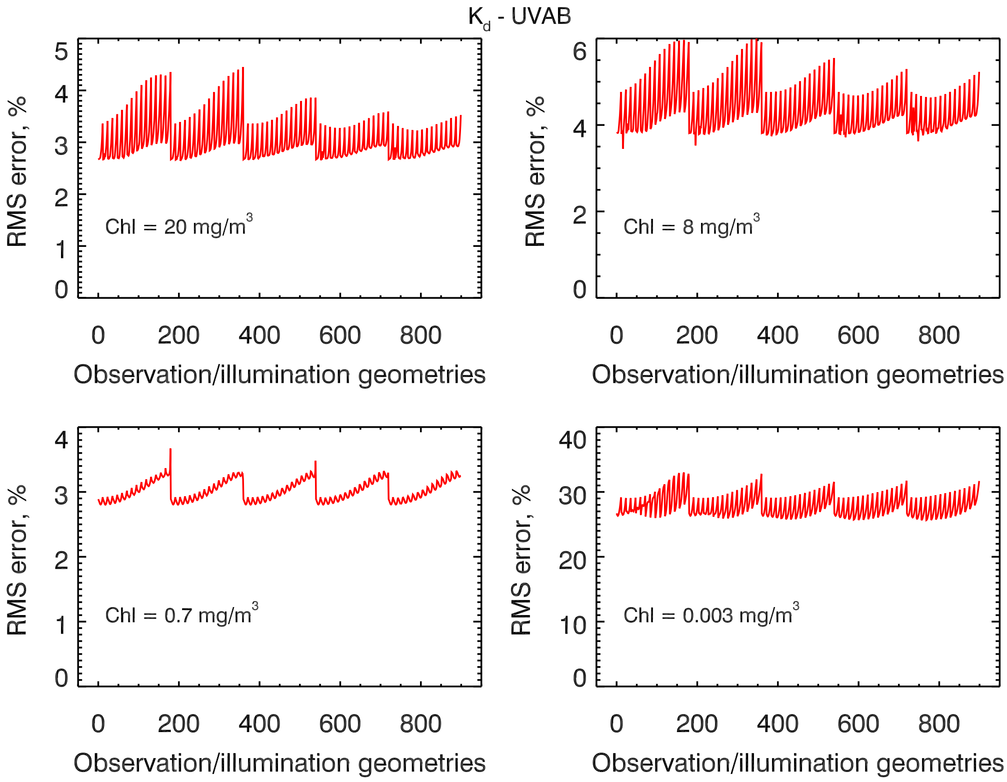

Figure 29: RMS errors of K_d UVAB for all viewing and solar angles (except of solar zenith angle 70°) and four selected concentrations of chlorophyll. Upper panel: left - 20 mg/m^3; right - 8 mg/m^3. Lower panel: left - 0.7 mg/m^3; right - 0.003 mg/m^3.

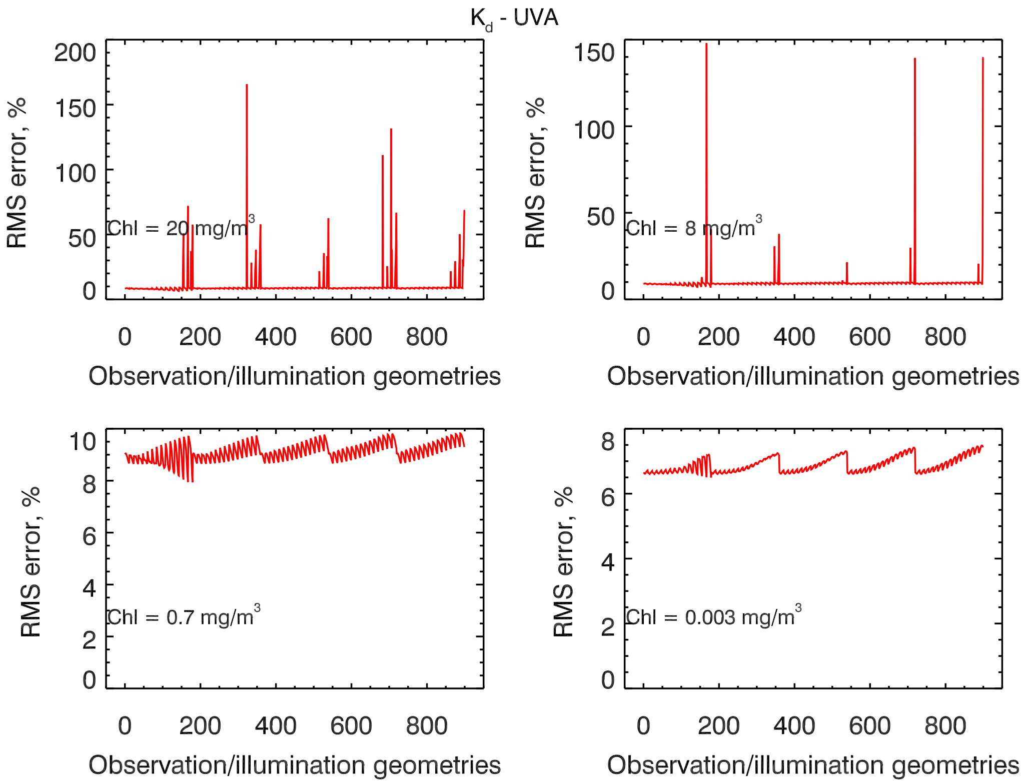

Figure 30: RMS errors of K_d UVA for all viewing and solar angles (except of solar zenith angle 70°) and four selected concentrations of chlorophyll. Upper panel: left - 20 mg/m^3; right - 8 mg/m^3. Lower panel: left - 0.7 mg/m^3; right - 0.003 mg/m^3.

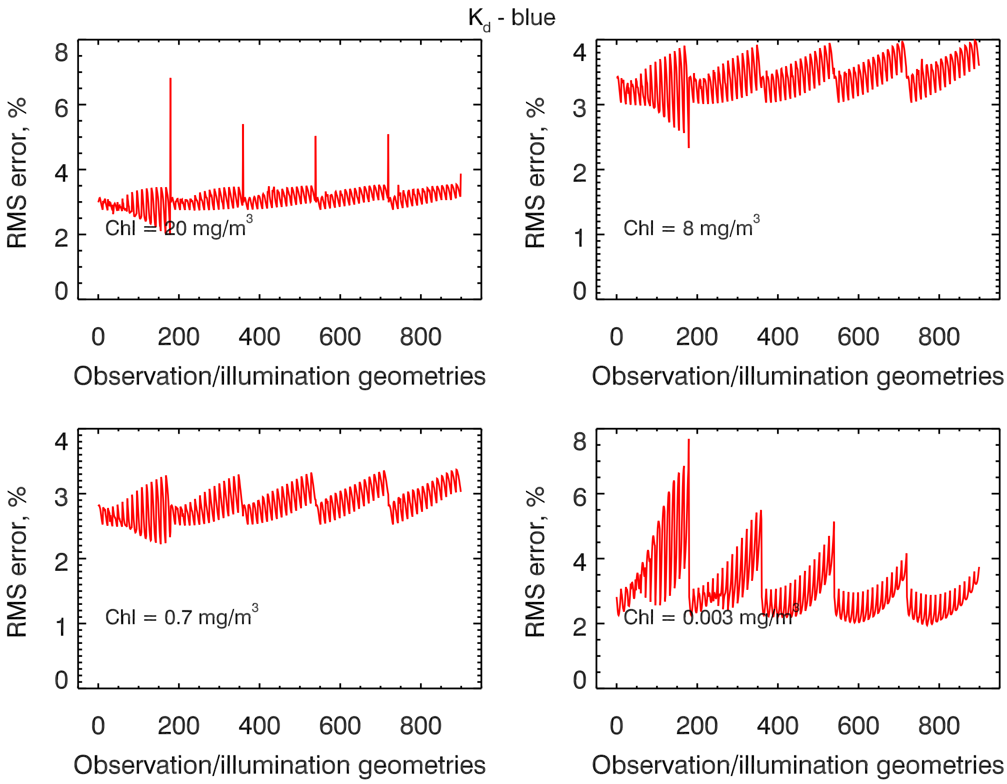

Figure 31: RMS errors of K_d short-blue for all viewing and solar angles (except of solar zenith angle 70°) and four selected concentrations of chlorophyll. Upper panel: left - 20 mg/m^3; right - 8 mg/m^3. Lower panel: left - 0.7 mg/m^3; right - 0.003 mg/m^3.

III Impact of interpolation of K$_d$ LUTs values

Taking into account that a measured VRS fit factor can be obtained for solar and viewing angles which do not coincide with the angle grids of LUTs, one needs to interpolate Kd LUTs values. In order to estimate interpolation errors we have calculated TOA radiances using shifted angles grid. The following subsections present results obtained using the shift of solar, viewing zenith, and azimuth angles.

In general, one needs to keep in mind that the main LUTs were precalculated for discrete number of solar, viewing zenith, and azimuth angles. In follows the variable $\Omega_{ijk} := \{\vartheta_{0i}, \vartheta_j, \varphi_k\}$, which comprises these three angle variables, will be used. In particular,

ϑ_{0i}, $i = [1, 2, \ldots, 13]$ represents discrete number of solar angles, [10, 15, 20,. . . ,70]

ϑ_j, $j = [1, 2, \ldots, 15]$ represents discrete number of zenith angles, [0, 5, 10, ...,70],
φ_k, $k = [1, 2, \ldots, 5]$ represents discrete number of azimuth angles, [0, 45, 90, 135, 180].
For selected three angles the LUT can be represented from mathematic point of view as a nonlinear relationship:

$$\vec{K}_d(\Omega_{ijk}) \;=\; \Phi\,[\vec{S}_v(\Omega_{ijk})]\;, \tag{17}$$

where Φ is a nonlinear mapping, vectors $\vec{S}_v(\Omega_{ijk})$ and $\vec{K}_d(\Omega_{ijk})$ consist of 22 components of VRS fit factors and attenuation coefficients, respectively, corresponding to different concentrations of chlorophyll, 22 values of which were selected as [0.0, 0.001, 0.003, 0.005, 0.01, 0.03, 0.05, 0.1, 0.3, 0.5, 0.7, 0.8, 1.0, 1.5, 2.0, 3.0, 5.0, 8.0, 10.0, 15, 20, 30].

IIIa Shift of solar zenith angle

The shifted solar grid has been selected as follows: [12.5, 17.5, 22.5, ..., 67.5], and VRS fit factors, S_v, were calculated employing standard DOAS fit. Further we have assumed that for a selected shifted solar angle $\tilde{\vartheta}_{0i}$, which is located in $[\vartheta_{0i}, \vartheta_{0i+1}]$ range, the relationship between K_d and solar angle can be represented as a linear relationship:

$$K_d(\tilde{\vartheta}_{0i}) = a\,\tilde{\vartheta}_{0i} + b\;,\quad \tilde{\vartheta}_{0i} \in (\vartheta_{0i}, \vartheta_{0i+1})\;. \tag{18}$$

The coefficients a and b are given by

$$a = \frac{\tilde{K}_d(\Omega_{i+1jk}) - \tilde{K}_d(\Omega_{ijk})}{\vartheta_{0i+1} - \vartheta_{0i}}\;,\quad b = \frac{\tilde{K}_d(\Omega_{ijk})\,\vartheta_{0,i+1} - \tilde{K}_d(\Omega_{i+1jk})\,\vartheta_{0i}}{\vartheta_{0i+1} - \vartheta_{0i}}\;. \tag{19}$$

Here, $\tilde{K}_d(\Omega_{ijk})$ is calculated using a linear interpolation according to the following IDL INTERPOL function:

$$\log \tilde{K}_d(\Omega_{ijk}) = \mathrm{INTERPOL}(\vec{V}_i, \vec{X}_i, XOUT)\;, \tag{20}$$

where $\vec{V}_i = \log \vec{K}_d(\Omega_{ijk})$, $\vec{X}_i = \log \vec{S}_v(\Omega_{ijk})$, and $XOUT = \log S_v(\tilde{\vartheta}_{0i})$. The $\log K_d(\Omega_{i+1jk})$ value is obtained setting subscript $i+1$ instead of i in Eq. (20).

The calculations of $K_d(\tilde{\vartheta}_{0i})$ were performed for each selected $\tilde{\vartheta}_{0i}$ from shifted angles grid, and combination of all viewing zenith, azimuth angles and chlorophyll concentrations. Figs. 32 show relative deviation of derived $K_d(\tilde{\vartheta}_{0i})$ from expected K_d for K$_d$ -UVAB, K$_d$ -UVA, and K$_d$ -blue, respectively, for selected shifted solar angles.

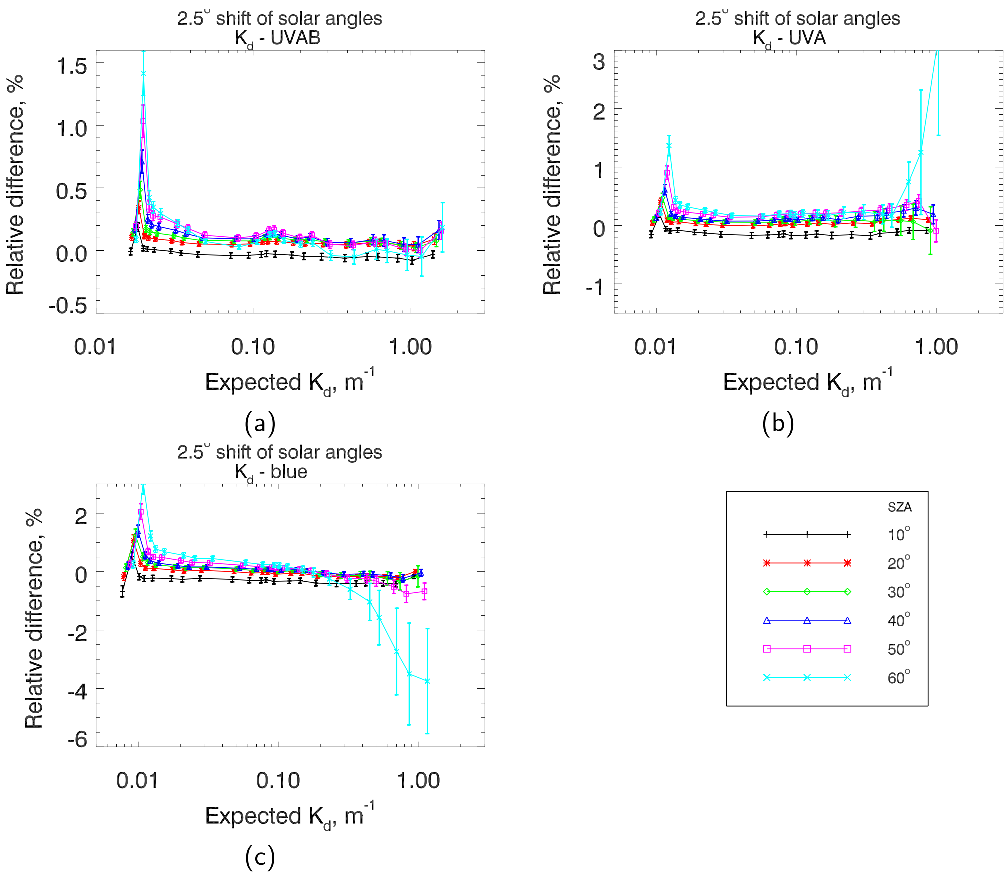

Figure 32: Deviation of derived from expected K_d in the case of 2.5° shift of the solar zenith angles. Results were averaged for different zenith and azimuth angles with the standard deviation given as errorbar.

The deviations of derived from expected K_d caused by interpolation of solar zenith angle are summarized in LUTs "Err_lut_W1.shi", "Err_lut_W2.shi", and "Err_lut_W3.shi" for "UVAB", "UVA" and "short-blue", respectively. In particular, the column 6 in these files contains the relative errors [%] caused by usage of 2.5° shifted solar angles in contrast to solar angles used in the main LUTs for K_d. The results of this column enable to obtain maximal error caused by interpolation with respect to solar zenith angle. We note that for a solar zenith angle $\tilde{\vartheta}_0 \in (\vartheta_{0i}, \vartheta_{0i+1})$ the maximal interpolation error is saved in LUTs corresponding to the solar zenith angle ϑ_{0i},.

IIIb Shift of viewing zenith angle

The shifted grid of viewing zenith angles has been selected as follows: [2.5, 7.5, 12.5,. . . , 67.5], and VRS fit factors, S_v, were calculated employing standard

DOAS fit. Simmiilar to the shift of solar angles grid we have assumed that for a selected shifted zenith angle $\tilde{\vartheta}_i$, which is located in $[\vartheta_i, \vartheta_{i+1}]$ range, the relationship between K_d and zenith angle can be represented as a local-linear relationship:

$$K_d(\tilde{\vartheta}_i) = a_\vartheta \, \tilde{\vartheta}_i + b_\vartheta \ , \quad \tilde{\vartheta}_i \in (\vartheta_i, \vartheta_{i+1}) \ . \tag{21}$$

The coefficients a_ϑ and b_ϑ are given by

$$a_\vartheta = \frac{\tilde{K}_d(\Omega_{ij+1k}) - \tilde{K}_d(\Omega_{ijk})}{\vartheta_{j+1} - \vartheta_j} \ , \quad b_\vartheta = \frac{\tilde{K}_d(\Omega_{ijk}) \, \vartheta_{j+1} - \tilde{K}_d(\Omega_{ij+1k}) \, \vartheta_j}{\vartheta_{j+1} - \vartheta_j} \ . \tag{22}$$

Here, $\tilde{K}_d(\Omega_{ijk})$ is calculated using a linear interpolation similar to Eq. (20), where, however, $XOUT = \log S_v(\tilde{\vartheta}_i)$. The $\log \tilde{K}_d(\Omega_{ij+1k})$ value is obtained setting subscript $j+1$ instead of j in Eq. (20).
The calculations of $K_d(\tilde{\vartheta}_i)$ were performed for each selected $\tilde{\vartheta}_i$ from shifted zenith angles grid, and combination of all solar, azimuth angles and chlorophyll concentrations. Figs. 33 show relative deviation of derived $K_d(\tilde{\vartheta})$ from expected K_d for K$_d$ -UVAB, K$_d$ -UVA, and K$_d$ -blue, respectively, for selected solar angles.

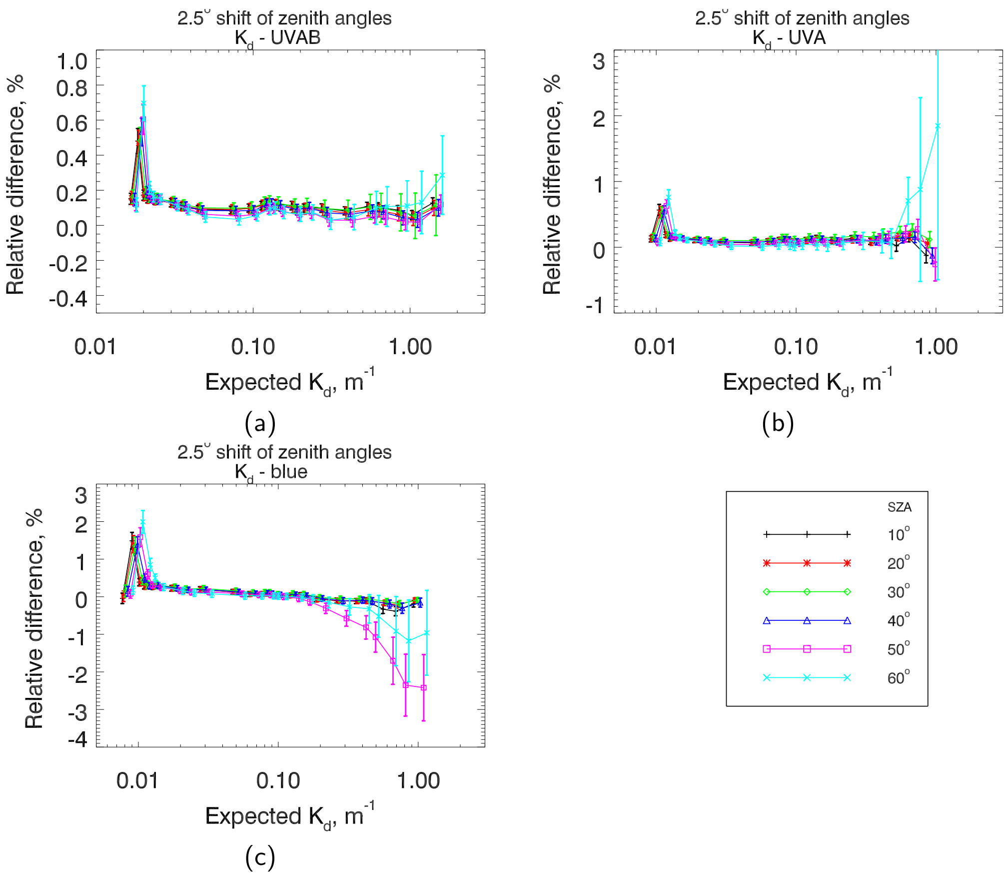

Figure 33: Deviation of derived from expected K_d in the case of 2.5° shift of viewing zenith angles. Results were averaged for different zenith and azimuth angles with the standard deviation given as errorbar.

The deviations of derived from expected K$_d$ caused by interpolation of VZA are summarized in LUTs "Err_lut_W1.shi", "Err_lut_W2.shi", and "Err_lut_W3.shi" for "UVAB", "UVA", and "short-blue", respectively.
In particular, the column 7 in these files contains the relative errors [%] caused by usage of 2.5° shifted VZAs in contrast to viewing angles used in the main LUTs for K_d. The results from this column enable to obtain maximal error caused by interpolation with respect to VZA. We note that for a viewing zenith angle $\tilde{\vartheta}_j \in (\vartheta_j, \vartheta_{j+1})$ the maximal interpolation error is saved at LUT corresponding to VZA ϑ_j.

IIIc Shift of azimuth angle

The shifted grid of azimuth angles has been selected as follows: [22.5, 67.5, 112.5, 157.5], and VRS fit factors, S_φ, were calculated employing standard DOAS fit. Similar to the shift of solar angles grid we have assumed that for a selected shifted azimuth angle $\tilde{\varphi}_i$, which is located in $[\varphi_i, \varphi_{i+1}]$ range, the relationship between K_d and azimuth angle can be represented as a linear relationship:

$$K_d(\tilde{\varphi}_i) = a_\varphi \, \tilde{\varphi}_i + b_\varphi \ , \quad \tilde{\varphi}_i \in (\varphi_i, \varphi_{i+1}) \ . \tag{23}$$

The coefficients a_φ and b_φ are given by

$$a_\varphi = \frac{\tilde{K}_d(\Omega_{ijk+1}) - \tilde{K}_d(\Omega_{ijk})}{\varphi_{k+1} - \varphi_k} \ , \quad b_\varphi = \frac{\tilde{K}_d(\Omega_{ijk}) \, \varphi_{k+1} - \tilde{K}_d(\Omega_{ijk+1}) \, \varphi_k}{\varphi_{k+1} - \varphi_k} \ . \tag{24}$$

Here, $\tilde{K}_d(\Omega_{ijk})$ is calculated using a linear interpolation similar to Eq. (20), where, however, $XOUT = \log S_\varphi(\tilde{\varphi}_i)$. The $\log \tilde{K}_d(\Omega_{ijk+1})$ value is obtained setting subscript $k+1$ instead of k in Eq. (20).
The calculations of $K_d(\tilde{\varphi}_i)$ were performed for each selected $\tilde{\varphi}_i$ from shifted angles grid, and combination of all zenith, azimuth angles and chlorophyll concentrations. Figs. 34 show relative deviation of derived $K_d(\tilde{\varphi})$ from expected K_d for K$_d$ -UVAB, K$_d$ -UVA, and K$_d$ -blue, respectively, for selected shifted azimuth angles.

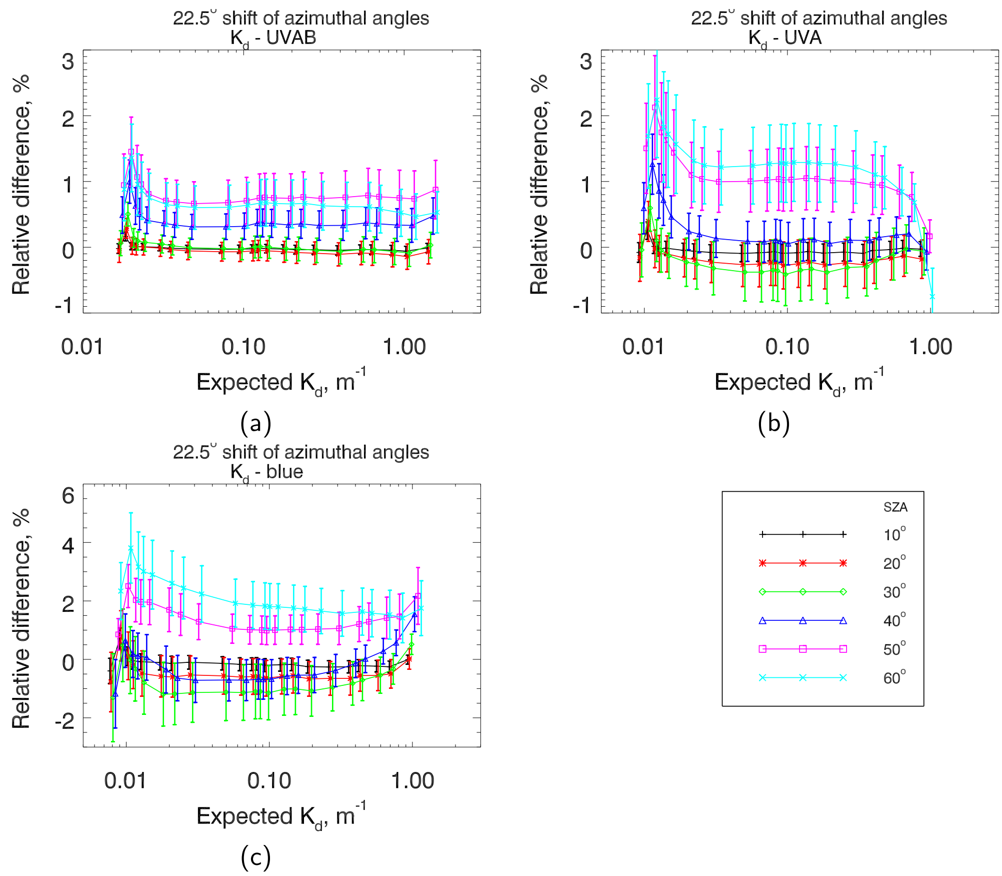

Figure 34: Deviation of derived from expected K_d in the case of 22.5° shift of azimuth angles. Results were averaged for different zenith and azimuth angles with the standard deviation given as errorbar.

The deviations of derived from expected K$_d$ caused by interpolation of azimuth angle are presented in LUTs "Err_lut_W1.shi", "Err_lut_W2.shi", and "Err_lut_W3.shi" for "UVAB", "UVA", and "short-blue", respectively. In particular, the column 8 in these files contains the relative errors [%] caused by usage of 22.5° shifted azimuth angles in contrast to azimuth angles used in main LUTs for K_d. The results from this column enable to obtain maximal error caused by interpolation with respect to azimuth angle. We note that for an azimuth angle $\tilde{\varphi}_k \in (\varphi_k, \varphi_{k+1})$ the maximal interpolation error is saved at LUT corresponding to the azimuth angle φ_k,.

6.2 Comparison to multispectral ocean color products

S5P ocean color product quality is estimated using triple collocation method as in Losa *et al.* (2017). Following data sets are used for the different products:

- S5P K_d blue, OLCI K_d 490 (empirical, Morel *et al.*, 2007), OC-CCI K_d 490 (IOP-based, Lee *et al.*, 2005)

More details on the multispectral products can be found in the S5POC VR.

6.2.1 Triple collocation

The triple collocation (TC) method (Stoffelen, 1998; Losa *et al.*, 2017) allows to estimate the absolute error variances ($\sigma^2_{\varepsilon_i}$), also called root mean squared difference (RMSD), of three collocated data sets with unknown uncertainties and with uncorrelated errors. The $\sigma^2_{\varepsilon_i}$ can be estimated from the unique terms covariance matrix (McColl *et al.*, 2014) (Q_{11}, Q_{12}, Q_{13}, Q_{22}, Q_{23},Q_{33}):

$$\sigma^2_{\varepsilon_i} = \begin{bmatrix} \sqrt{Q_{11} - \frac{Q_{12}Q_{13}}{Q_{23}}} \\ \sqrt{Q_{22} - \frac{Q_{12}Q_{23}}{Q_{13}}} \\ \sqrt{Q_{33} - \frac{Q_{13}Q_{23}}{Q_{12}}} \end{bmatrix} \tag{25}$$

Following Gruber *et al.* (2015) the fractional mean-squared-error (fMSE) can be calculated within the frame of the TC analysis:

$$fMSE_i = \frac{\sigma^2_{\varepsilon_i}}{\sigma^2_i} = \frac{1}{\beta^2_i \sigma^2_\Theta + \sigma^2_{\varepsilon_i}} = \frac{1}{1 + SNR_i}, \tag{26}$$

where β_i is a systematic bias of a particular data product with respect to the true state Θ; σ^2_i and $\sigma^2_{\varepsilon_i}$ denote the product variance and the product error variance, respectively. SNR_i is a signal-to-noise ratio. This fMSE criterion allows one to evaluate the plausibility of the TC based K_d uncertainty estimates. All details on the K_d triple collocation results can be found in the S5POC-VR (sections 6.1.5 to 6.1.8).

6.3 in-situ data

see section 7.

7 Validation

Table 1 summarizes information on *in situ* observations collected during cruises (PS113, PS121, MSM93) and surveys (FOCUS) in the test areas (Figure 2 in S5POC-RB, Figure A1 in S5POC-DP-AUM2) and used for S5POC product validation for the years 2018 to 2020. All details on the in validation results can be found in section 6.1.5 to 6.1.8 of the S5POC-VR (Bracher *et al.*, 2022b).

Table 1: *In situ* observations used for S5POC evaluation.

Observation name	observation description	cruises/survey	test area
K_d	Light attenuation	PS113, PS121, MSM93	C, D

7.1 Match-up analyses

Collocations between *In situ* and S5POC products were defined differently for the products. Match-ups between geolocation of *in situ* and TROPOMI ground pixels for S5POC K_d data were calculated using a loose criterion (within two days of the TROPOMI pixel) given the low number of regional available K_d *in situ* station data (in total 36 station data regional well distributed) complemented by about 450 Triaxus data. For each *in situ* measurement, TROPOMI match-ups were searched within 2 days and a radius of 5.5 km resulting in 45 (only 43 for UVAB) quality controlled matchups. For details see section 6.2.2 of the Bracher *et al.* (2022b).

The match-up statistics are quantified by the metrics described in the OC-CCI Product User Guide (issue 2.0.5). The metrics includes RMSD, un-biased RMSD, bias, slope, intercept (type II regression) and Pearson coefficient of determination. In addition, the mean absolute error (MAE) is quantified. The metrics are computed as:

$$\text{RMSD} = \sqrt{\frac{1}{N}\sum_{i=1}^{N}(y_i - x_i)^2} \tag{27}$$

$$\text{Un-biased RMSD} = \sqrt{\frac{1}{N}\sum_{i=1}^{N}(Y_i - X_i)^2} \tag{28}$$

$$\text{Bias} = \frac{1}{N}\sum_{i=1}^{N}(y_i - x_i) \tag{29}$$

$$\text{MAE} = \frac{1}{N}\sum_{i=1}^{N}|y_i - x_i| \tag{30}$$

where x is the *in situ* observation, y the satellite data, and N the total number of samples. X corresponds to $x - mean(x)$ and analogous definition applies to Y. For PFT-CHL for the calculation of slope, intercept (type II regression) and Pearson coefficient of determination the PFT-CHL from *in situ* and TROPOMI are compared on Log10 scale. More details on the *in situ* matchup results can be found in sections 6.1.2 and 6.2.2 of S5POC-VR (Bracher *et al.*, 2022b)).

References

Austin, R. W., & Petzold, T. J. 1981. *The Determination of the Diffuse Attenuation Coefficient of Sea Water Using the Coastal Zone Color Scanner.* Boston, MA: Springer US. Pages 239–256.

Blum, M, Rozanov, V V, Burrows, J P, & Bracher, A. 2012. Coupled ocean-atmosphere radiative transfer model in the framework of software package SCIATRAN: Selected comparisons to model and satellite data. *Advances in Space Research*, **49**(12), 1728–1742.

Bracher, A, Vountas, M, Dinter, T, Burrows, J P, Röttgers, R, & Peeken, I. 2009. Quantitative observation of cyanobacteria and diatoms from space using PhytoDOAS on SCIAMACHY data. *Biogeosciences*, **6**(5), 751–764.

Bracher, A., Alvarado, L., Richter, A., Brotas, V., Brito, A., & Costa, M. 2022a. *Sentinel-5P Ocean Colour: Impact Assessment. S5POC-IAR-D09 Version 1.1. 13 May 2022.* Tech. rept. Alfred Wegener Institute Helmholtz Centre for Polar and Marine Research; Institute of Environmental Physics, University of Bremen; Faculdade de Ciencias, Universidade de Lisboa; University of Victoria.

Bracher, A., Losa, S., Brotas, V., Oelker, J., Rio, M.-H., & Xi, H. 2022b. *Sentinel-5P Ocean Colour: Validation Report. S5POC VR Version 3.1. 13 May 2022.* Tech. rept. Alfred Wegener Institute (AWI), Helmholtz Centre for Polar and Marine Research; Institute of Environmental Physics, University of Bremen; Faculdade de Ciencias, Universidade de Lisboa.

Bracher, Astrid U., & Wiencke, Christian. 2000. Simulation of the effects of naturally enhanced UV radiation on photosynthesis of Antarctic phytoplankton. *Marine Ecology Progress Series*, **196**, 127–141.

Chance, K, & Kurucz, R L. 2010. An improved high-resolution solar reference spectrum for earth's atmosphere measurements in the ultraviolet, visible, and near infrared. *Journal of Quantitative Spectroscopy and Radiative Transfer*, **111**(9), 1289–1295.

Dinter, T, Rozanov, V V, Burrows, J P, & Bracher, A. 2015. Retrieving the availability of light in the ocean utilising spectral signatures of vibrational Raman scattering in hyper-spectral satellite measurements. *Ocean Science*, **11**(3), 373–389.

Gordon, Howard R, & McCluney, W R. 1975. Estimation of the Depth of Sunlight Penetration in the Sea for Remote Sensing. *Appl. Opt.*, **14**(2), 413–416.

Grainger, J F, & Ring, J. 1962. Anomalous Fraunhofer Line Profiles. *Nature*, **193**(feb), 762.

Gruber, A., Su, C.-H., Zwieback, S., Crow, W., Dorigo, W., & Wagner, W. 2015. Recent advances in (soil moisture) triple collocation analysis. *International Journal of Applied Earth Observation and Geoinformation.*

Haltrin, Vladimir I, & Kattawar, George W. 1993. Self-consistent solutions to the equation of transfer with elastic and inelastic scattering in oceanic optics: I. Model. *Appl. Opt.*, **32**(27), 5356–5367.

Joiner, J, & Vasilkov, A P. 2006. First results from the OMI rotational Raman scattering cloud pressure algorithm. *IEEE Transactions on Geoscience and Remote Sensing*, **44**(5), 1272–1282.

Lee, Zhong-Ping, Du, Ke-Ping, & Arnone, Robert. 2005. A model for the diffuse attenuation coefficient of downwelling irradiance. *Journal of Geophysical Research: Oceans*, **110**(C2), C02016.

Losa, Svetlana N, Soppa, Mariana A, Dinter, Tilman, Wolanin, Aleksandra, Brewin, Robert J W, Bricaud, Annick, Oelker, Julia, Peeken, Ilka, Gentili, Bernard, Rozanov, Vladimir, & Bracher, Astrid. 2017. Synergistic Exploitation of Hyper- and Multi-Spectral Precursor Sentinel Measurements to Determine Phytoplankton Functional Types (SynSenPFT). *Frontiers in Marine Science*, **4**, 203.

Mason, John D, Cone, Michael T, & Fry, Edward S. 2016. Ultraviolet (250–550 nm) absorption spectrum of pure water. *Appl. Opt.*, **55**(25), 7163–7172.

McColl, Kaighin A, Vogelzang, Jur, Konings, Alexandra G, Entekhabi, Dara, Piles, María, & Stoffelen, Ad. 2014. Extended triple collocation: Estimating errors and correlation coefficients with respect to an unknown target. *Geophysical Research Letters*, **41**(17), 6229–6236.

Mobley, C.D., & Sundman, L.K. 2013. *HydroLight 5.2 - EcoLight 5.2 Technical Documentation*. Tech. rept. Sequoia Scientific, Inc.

Morel, André. 1988. Optical modeling of the upper ocean in relation to its biogenous matter content (case I waters). *Journal of Geophysical Research: Oceans*, **93**(C9), 10749–10768.

Morel, André, & Maritorena, Stéphane. 2001. Bio-optical properties of oceanic waters: A reappraisal. *Journal of Geophysical Research: Oceans*, **106**(C4), 7163–7180.

Morel, André, Huot, Yannick, Gentili, Bernard, Werdell, P. Jeremy, Hooker, Stanford B., & Franz, Bryan A. 2007. Examining the consistency of products derived from various ocean color sensors in open ocean (Case 1) waters in the perspective of a multi-sensor approach. *Remote Sensing of Environment*, **111**(1), 69 – 88.

Oelker, J. 2021. *PhD Thesis*. Bremen: Department of Physics and Engineering, University Bremen, Bremen, Germany.

Oelker, J., L., Alvarado, & Bracher, A. 2022a. *Sentinel-5P Ocean Colour: Product User Manual. S5POC-PUM D07 Version 3.1. 13 May 2022.* Tech. rept. Alfred-Wegener Institut Helmholtz Zentrum fuer Polar- und Meeresforschung, and IUP, University Bremen.

Oelker, Julia, Richter, Andreas, Dinter, Tilman, Rozanov, Vladimir V., Burrows, John P., & Bracher, Astrid. 2019. Global diffuse attenuation derived from vibrational Raman scattering detected in hyperspectral backscattered satellite spectra. *Opt. Express*, **27**(12), A829–A855.

Oelker, Julia, Losa, Svetlana N., Richter, Andreas, & Bracher, Astrid. 2022b. TROPOMI-Retrieved Underwater Light Attenuation in Three Spectral Regions in the Ultraviolet and Blue. *Frontiers in Marine Science*, **9**.

O'Reilly, John E., Maritorena, Stéphane, Mitchell, B. Greg, Siegel, David A., Carder, Kendall L., Garver, Sara A., Kahru, Mati, & McClain, Charles. 1998. Ocean color chlorophyll algorithms for SeaWiFS. *Journal of Geophysical Research: Oceans*, **103**(C11), 24937–24953.

Perner, D, & Platt, U. 1979. Detection of nitrous acid in the atmosphere by differential optical absorption. *Geophysical Research Letters*, **6**(12), 917–920.

Pope, Robin M., & Fry, Edward S. 1997. Absorption spectrum (380–700 nm) of pure water. II. Integrating cavity measurements. *Appl. Opt.*, **36**(33), 8710–8723.

Remer, Lorraine A, Kleidman, Richard G, Levy, Robert C, Kaufman, Yoram J, Tanré, Didier, Mattoo, Shana, Martins, J Vanderlei, Ichoku, Charles, Koren, Ilan, Yu, Hongbin, & Holben, Brent N. 2008. Global aerosol climatology from the MODIS satellite sensors. *Journal of Geophysical Research: Atmospheres*, **113**(D14), D14S07.

Rothman, L S, Gordon, I E, Babikov, Y, Barbe, A, Benner, D Chris, Bernath, P F, Birk, M, Bizzocchi, L, Boudon, V, Brown, L R, Campargue, A, Chance, K, Cohen, E A, Coudert, L H, Devi, V M, Drouin, B J, Fayt, A, Flaud, J.-M., Gamache, R R, Harrison, J J, Hartmann, J.-M., Hill, C, Hodges, J T, Jacquemart, D, Jolly, A, Lamouroux, J, Roy, R J Le, Li, G, Long, D A, Lyulin, O M, Mackie, C J, Massie, S T, Mikhailenko, S, Müller, H S P, Naumenko, O V, Nikitin, A V, Orphal, J, Perevalov, V, Perrin, A, Polovtseva, E R, Richard, C, Smith, M A H, Starikova, E, Sung, K, Tashkun, S, Tennyson, J, Toon, G C, Tyuterev, Vl.G., & Wagner, G. 2013. The HITRAN2012 molecular spectroscopic database. *Journal of Quantitative Spectroscopy and Radiative Transfer*, **130**, 4–50.

Rozanov, V V, Rozanov, A V, Kokhanovsky, A A, & Burrows, J P. 2014. Radiative transfer through terrestrial atmosphere and ocean: Software package SCIATRAN. *Journal of Quantitative Spectroscopy and Radiative Transfer*, **133**, 13–71.

Rozanov, V V, Dinter, T, Rozanov, A V, Wolanin, A, Bracher, A, & Burrows, J P. 2017. Radiative transfer modeling through terrestrial atmosphere and ocean accounting for inelastic processes: Software package SCIATRAN. *Journal of Quantitative Spectroscopy and Radiative Transfer*, **194**, 65–85.

Sadeghi, A, Dinter, T, Vountas, M, Taylor, B B, Altenburg-Soppa, M, Peeken, I, & Bracher, A. 2012. Improvement to the PhytoDOAS method for identification of coccolithophores using hyper-spectral satellite data. *Ocean Science*, **8**(6), 1055–1070.

Serdyuchenko, A, Gorshelev, V, Weber, M, Chehade, W, & Burrows, J P. 2014. High spectral resolution ozone absorption cross-sections – Part 2: Temperature dependence. *Atmospheric Measurement Techniques*, **7**(2), 625–636.

Stoffelen, Ad. 1998. Toward the true near-surface wind speed: Error modeling and calibration using triple collocation. *Journal of Geophysical Research: Oceans (1978–2012)*, **103**(C4), 7755–7766.

Thalman, Ryan, & Volkamer, Rainer. 2013. Temperature dependent absorption cross-sections of O2–O2 collision pairs between 340 and 630 nm and at atmospherically relevant pressure. *Phys. Chem. Chem. Phys.*, **15**(37), 15371–15381.

van der Does, M., Korte, L. F., Munday, C. I., Brummer, G.-J. A., & Stuut, J.-B. W. 2016. Particle size traces modern Saharan dust transport and deposition across the equatorial North Atlantic. *Atmospheric Chemistry and Physics*, **16**(21), 13697–13710.

van Geffen, J, Eskes, H, K., Boersma, J., Maasakkers, & Veefkind, J. 2019. *TROPOMI ATBD of the total and tropospheric NO2 data products Technical Report*. Tech. rept. Royal Netherlands Meteorological Institute.

Vandaele, A.C., Hermans, C., Simon, P.C., Carleer, M., Colin, R., Fally, S., Mérienne, M.F., Jenouvrier, A., & Coquart, B. 1998. Measurements of the NO2 absorption cross-section from 42 000 cm–1 to 10 000 cm–1 (238–1000 nm) at 220 K and 294 K. *Journal of Quantitative Spectroscopy and Radiative Transfer*, **59**(3), 171 – 184. Atmospheric Spectroscopy Applications 96.

Vasilkov, Alexander P, Joiner, Joanna, Gleason, James, & Bhartia, Pawan K. 2002. Ocean Raman scattering in satellite backscatter UV measurements. *Geophysical Research Letters*, **29**(17), 14–18.

Veefkind, J.P., Aben, I., McMullan, K., Förster, H., de Vries, J., Otter, G., Claas, J., Eskes, H.J., de Haan, J.F., Kleipool, Q., van Weele, M., Hasekamp, O., Hoogeveen, R., Landgraf, J., Snel, R., Tol, P., Ingmann, P., Voors, R., Kruizinga, B., Vink, R., Visser, H., & Levelt, P.F. 2012. TROPOMI on the ESA Sentinel-5 Precursor: A GMES mission for global observations of the atmospheric composition for climate, air quality and ozone layer applications. *Remote Sensing of Environment*, **120**, 70 – 83. The Sentinel Missions - New Opportunities for Science.

Vernet, Maria, Brody, Eric A., Holm-Hansen, Osmund, & Mitchell, B. Greg. 1994. *The Response of Antarctic Phytoplankton to Ultraviolet Radiation: Absorption, Photosynthesis, and Taxonomic Composition*. American Geophysical Union (AGU). Pages 143–158.

Vodacek, A., Blough, N., DeGrandpre, M., & Nelson, R. 1997. Seasonal variation of CDOM and DOC in the Middle Atlantic Bight: Terrestrial inputs and photooxidation. *Limnology and Oceanography*, **42**, 674–686.

Vountas, M, Rozanov, VV, & Burrows, JP. 1998. Ring effect: Impact of rotational Raman scattering on radiative transfer in Earth's atmosphere. *Journal of Quantitative Spectroscopy and Radiative Transfer*, **60**(6), 943–961.

Vountas, M, Richter, A, Wittrock, F, & Burrows, J P. 2003. Inelastic scattering in ocean water and its impact on trace gas retrievals from satellite data. *Atmospheric Chemistry and Physics*, **3**(5), 1365–1375.

Vountas, M, Dinter, T, Bracher, A, Burrows, J P, & Sierk, B. 2007. Spectral studies of ocean water with space-borne sensor SCIAMACHY using Differential Optical Absorption Spectroscopy (DOAS). *Ocean Science*, **3**(3), 429–440.

Walrafen, G E. 1967. Raman Spectral Studies of the Effects of Temperature on Water Structure. *The Journal of Chemical Physics*, **47**(1), 114–126.

Wang, Yongchao, Lee, Z., Wei, Jianwei, Shang, S., Wang, M., & Lai, Wendian. 2021. Extending satellite ocean color remote sensing to the near-blue ultraviolet bands. *Remote Sensing of Environment*, **253**, 112228.

Wolanin, A, Rozanov, V V, Dinter, T, Noël, S, Vountas, M, Burrows, J P, & Bracher, A. 2015a. Global retrieval of marine and terrestrial chlorophyll fluorescence at its red peak using hyperspectral top of atmosphere radiance measurements: Feasibility study and first results. *Remote Sensing of Environment*, **166**, 243–261.

Wolanin, A., Dinter, T., Soppa, M., & Bracher, A. 2015b. *Report on using radiative transfer modeling to develop a correction scheme and investigate the sensitivity of the improved PhytoDOAS (version3.0) algorithm. SY-4Sci Synergy R & D Study 4: Phytoplankton Functional Types (SynSenPFT)*. Tech. rept. Alfred Wegener Institute (AWI), Helmholtz Centre for Polar and Marine Research; Institute of Environmental Physics, University of Bremen.

*** END OF DOCUMENT ***